

Phase transitions in fluctuations and their role in two-step nucleation ^{EP}

Cite as: J. Chem. Phys. **150**, 074501 (2019); <https://doi.org/10.1063/1.5057429>

Submitted: 14 September 2018 . Accepted: 16 January 2019 . Published Online: 20 February 2019

Daniella James, Seamus Beairstó ^{id}, Carmen Hartt, Oleksandr Zavalov ^{id}, Ivan Saika-Voivod ^{id}, Richard K. Bowles ^{id}, and Peter H. Poole ^{id}

COLLECTIONS

Paper published as part of the special topic on [JCP Editors' Choice 2019](#)

^{EP} This paper was selected as an Editor's Pick



View Online



Export Citation



CrossMark

ARTICLES YOU MAY BE INTERESTED IN

[Nucleation in aqueous NaCl solutions shifts from 1-step to 2-step mechanism on crossing the spinodal](#)

The Journal of Chemical Physics **150**, 124502 (2019); <https://doi.org/10.1063/1.5084248>

[Thermodynamic picture of vitrification of water through complex specific heat and entropy: A journey through “no man’s land”](#)

The Journal of Chemical Physics **150**, 054502 (2019); <https://doi.org/10.1063/1.5079594>

[Advances in the experimental exploration of water’s phase diagram](#)

The Journal of Chemical Physics **150**, 060901 (2019); <https://doi.org/10.1063/1.5085163>

Lock-in Amplifiers

Find out more today



Zurich
Instruments

Phase transitions in fluctuations and their role in two-step nucleation

Cite as: J. Chem. Phys. 150, 074501 (2019); doi: 10.1063/1.5057429

Submitted: 14 September 2018 • Accepted: 16 January 2019 •

Published Online: 20 February 2019



View Online



Export Citation



CrossMark

Daniella James,¹ Seamus Beairsto,¹  Carmen Hartt,¹ Oleksandr Zavalov,¹  Ivan Saika-Voivod,² 
Richard K. Bowles,³  and Peter H. Poole¹ 

AFFILIATIONS

¹Department of Physics, St. Francis Xavier University, Antigonish, Nova Scotia B2G 2W5, Canada

²Department of Physics and Physical Oceanography, Memorial University of Newfoundland, St. John's, Newfoundland A1B 3X7, Canada

³Department of Chemistry, University of Saskatchewan, Saskatoon, Saskatchewan S7N 5C9, Canada

ABSTRACT

We consider the thermodynamic behavior of local fluctuations occurring in a stable or metastable bulk phase. For a system with three or more phases, we present a simple analysis based on classical nucleation theory that predicts thermodynamic conditions at which small fluctuations resemble the phase having the lowest surface tension with the surrounding bulk phase, even if this phase does not have a lower chemical potential. We also identify the conditions at which a fluctuation may convert to a different phase as its size increases, referred to here as a “fluctuation phase transition” (FPT). We demonstrate these phenomena in simulations of a two dimensional lattice model by evaluating the free energy surface that describes the thermodynamic properties of a fluctuation as a function of its size and phase composition. We show that a FPT can occur in the fluctuations of either a stable or metastable bulk phase and that the transition is first-order. We also find that the FPT is bracketed by well-defined spinodals, which place limits on the size of fluctuations of distinct phases. Furthermore, when the FPT occurs in a metastable bulk phase, we show that the superposition of the FPT on the nucleation process results in two-step nucleation (TSN). We identify distinct regimes of TSN based on the nucleation pathway in the free energy surface and correlate these regimes to the phase diagram of the bulk system. Our results clarify the origin of TSN and elucidate a wide variety of phenomena associated with TSN, including the Ostwald step rule.

Published under license by AIP Publishing. <https://doi.org/10.1063/1.5057429>

I. INTRODUCTION

Fluctuations play a central role in many liquid state phenomena. For example, it has long been appreciated that fluctuations dominate the physics of critical phenomena and second-order phase transitions.¹ Similarly, in the study of supercooled liquids and the origin of the glass transition, local fluctuations that deviate from the average properties of the bulk liquid phase (e.g., dynamical heterogeneities and locally favored structures) continue to be the focus of much work to explain the complex dynamics observed as a liquid transforms to an amorphous solid.^{2–4} For network-forming liquids such as water, “two-state” models that assume the occurrence of two distinct, transient local structures have been proposed to explain thermodynamic and dynamic anomalies

occurring in both the stable and supercooled liquids.⁵ The central role of fluctuations is perhaps most obvious in nucleation phenomena, where a bulk metastable phase decays to a stable phase via the formation of a local fluctuation (the critical nucleus) of sufficient size to be able to grow spontaneously to a macroscopic scale.^{6,7}

The behavior of local fluctuations is particularly complex in the case of “two-step nucleation” (TSN).^{8–41} In TSN, the first step in the phase transformation process consists of the appearance in the bulk metastable phase of a local fluctuation that resembles an intermediate phase distinct from the stable phase. In the second step of TSN, this intermediate fluctuation undergoes a transition in which the stable phase emerges from within the intermediate phase. Evidence for TSN has been observed experimentally in a wide range of

molecular and colloidal systems,^{10,18,28,34} including important cases relevant to understanding protein crystallization^{39,40} and biomineralization.^{15,16} Due to the involvement of an intermediate phase, TSN is poorly described by classical nucleation theory (CNT), in which it is assumed that a nucleus of the stable phase appears directly from the metastable phase.^{6,7} Large deviations from CNT predictions are thus associated with TSN.²³ Given these challenges, an understanding of TSN is required to better control and exploit complex nucleation phenomena. For example, significant questions remain concerning the nature of long-lived “pre-nucleation clusters” that have been reported in some TSN processes.^{15,16,22,27} Control of polymorph selection during nucleation and the origins of the Ostwald step rule (OSR)⁷ are also facilitated by a better understanding of TSN.^{26,41,42}

A number of theoretical and simulation studies have investigated TSN.^{8,9,11–14,17,19–21,24–26,29,31–33,36,37,41} These studies highlight the role of metastable phase transitions involving competing bulk phases and their connection to the transition from the intermediate to the stable fluctuation that occurs in TSN. In addition, several studies have examined TSN in terms of the two dimensional (2D) free energy surface (FES) that quantifies the nucleation pathway as a function of the size of the nucleus and its degree of similarity to the stable phase.^{8,17,19–21,29,31,32} For example, Duff and Peters demonstrated the existence of two distinct regimes of TSN, in which the transition of the nucleus to the stable phase occurs either before or after the formation of the critical nucleus, located at the saddle point of the FES.¹⁷ Iwamatsu further showed that the FES for TSN may contain two distinct nucleation pathways, each with its own saddle point.²¹ These studies illustrate the complexity of TSN and help us to explain the non-classical phenomena attributed to TSN in experiments.

Despite the insights obtained to date from experiments, theory, and simulation, our understanding of TSN would benefit from a clearer understanding of the relationship between a bulk phase transition and the transition that occurs in the growing nucleus from the intermediate to the stable phase. This latter transition occurs in a finite-sized system (the fluctuation) and is controlled not only by the chemical potential difference between the intermediate and stable phases but also by strong surface effects at the interface with the surrounding bulk metastable phase. In the following, we refer to the transition that occurs in a finite-sized fluctuation as a “fluctuation phase transition” (FPT) to distinguish it from a bulk phase transition, for which surface effects play no role in determining the thermodynamic conditions of the equilibrium transition. It would be particularly useful to know how to predict the conditions at which a FPT will occur and how these conditions are related to the thermodynamic conditions at which bulk phase transitions, both stable and metastable, occur in the same system.

This paper has two aims: First, we seek to clarify the general thermodynamic behavior of local fluctuations, regardless of whether these fluctuations are involved in a nucleation process, to better understand the properties of fluctuations in their own right. Second, we wish to specifically elucidate TSN

via a detailed examination of the local fluctuations that appear during TSN and how the behavior of these fluctuations varies over a wide range of thermodynamic conditions.

To achieve these aims, we first present in Sec. II a simple theoretical analysis of fluctuations. This analysis uses the assumptions of classical nucleation theory (CNT) to make some general predictions on the nature of local fluctuations in either a stable or a metastable phase when more than one type of fluctuation is possible. This analysis identifies a number of distinct thermodynamic scenarios for how fluctuations behave as a function of their size, including predicting the conditions at which a FPT will occur.

In Secs. III–VI, we then describe simulations of a 2D lattice model, which provides a case study in which our analytical predictions can be tested. In particular, the model is simple enough to provide a complete thermodynamic description of the fluctuations, in the form of a FES which characterizes the fluctuations in terms of their size and phase composition. We locate and characterize the FPT as it is observed in the features of the FES for both a stable and metastable phase. Our lattice model results demonstrate that TSN occurs when a FPT is superimposed on a nucleation process occurring in a metastable phase. We are thus able to provide a comprehensive perspective on the origins of TSN, clarify its relationship to bulk phase behavior, and elucidate the non-classical nature of TSN.

In Sec. VII, we discuss the connections between our results and previous studies on TSN, such as Refs. 17 and 21. Our results reproduce a number of observations made previously in separate studies, as well as identifying new behavior that underlies these previous observations, thus unifying our understanding of the origins of TSN and related phenomena. At the same time, our results demonstrate that complex thermodynamic behavior is an intrinsic property of fluctuations, independent of metastability and nucleation. As discussed in Sec. VIII, our findings thus have wider implications for understanding liquid state phenomena that are dominated by the behavior of fluctuations.

II. CNT ANALYSIS OF FLUCTUATIONS

We begin with an idealized analysis of the fluctuations in a bulk phase when there are two other bulk phases that may occur in the system. As we will see, this analysis suggests the existence of several distinct regimes of fluctuation behavior depending on the thermodynamic conditions, including regimes in which a FPT occurs. Since some of these regimes also correspond to TSN processes, this analysis provides an idealized framework for understanding the origins of TSN. Furthermore, the analysis predicts a regime in which a FPT occurs in a stable phase where nucleation is not possible, demonstrating that a FPT and nucleation can be regarded as independent phenomena.

Consider the free energy cost G to create a fluctuation of size n molecules within a bulk phase \mathcal{A} . We assume that any such fluctuation can be associated with one of two other bulk phases \mathcal{B} or \mathcal{C} and that the temperature of the system is such that any bulk transition between phases is first order. We also

assume that the free energy cost to create a fluctuation of \mathcal{B} or \mathcal{C} within \mathcal{A} is given respectively by the CNT expressions,

$$\begin{aligned} G_{AB} &= n^\alpha \phi \sigma_{AB} + n \Delta\mu_{AB}, \\ G_{AC} &= n^\alpha \phi \sigma_{AC} + n \Delta\mu_{AC}, \end{aligned} \quad (1)$$

where σ_{AB} is the \mathcal{AB} surface tension and $\Delta\mu_{AB} = \mu_B - \mu_A$ is the difference in the chemical potential between the bulk phases \mathcal{B} and \mathcal{A} and where σ_{AC} and $\Delta\mu_{AC}$ are similarly defined.^{6,7} Here we assume that the surface area of the fluctuation is $n^\alpha \phi$, where $\alpha = (D - 1)/D$ depends on the dimension of space D and ϕ is a shape factor. For circular fluctuations in $D = 2$, $\alpha = 1/2$ and $\phi = (4\pi v)^{1/2}$, where v is the area per molecule. For spherical fluctuations in $D = 3$, $\alpha = 2/3$ and $\phi = (36\pi v^2)^{1/3}$, where v is the volume per molecule.

Let us now assume that the \mathcal{B} phase has a lower surface tension with \mathcal{A} than does \mathcal{C} , i.e., $\sigma_{AB} < \sigma_{AC}$. Six distinct cases are then possible for the relative behavior of G_{AB} and G_{AC} , corresponding to the six possible orderings of the chemical potentials μ_A , μ_B , and μ_C , as illustrated in Fig. 1. When the \mathcal{B} phase is more stable than \mathcal{C} [i.e., $\Delta\mu_{CB} = \mu_B - \mu_C < 0$, corresponding to panels (a)–(c) in Fig. 1], then G_{AB} is always lower than G_{AC} , and so the most probable fluctuations of \mathcal{A} remain \mathcal{B} -like for all n . However, when the \mathcal{C} phase is more stable than \mathcal{B} [i.e., $\Delta\mu_{CB} > 0$, corresponding to panels (d)–(f) in Fig. 1], G_{AB}

and G_{AC} will cross at a value of $n = n_c$ given by

$$n_c^{1/D} = \phi \frac{\sigma_{AC} - \sigma_{AB}}{\Delta\mu_{CB}}. \quad (2)$$

If $n_c > 1$, the minimum size of an observable fluctuation, this crossing will manifest itself as a FPT. That is, the fluctuation will resemble the \mathcal{B} phase when it first appears and then undergoes a transition to the \mathcal{C} phase as it grows.

Notably, in every panel of Fig. 1, the initial fluctuation is \mathcal{B} -like. That is, the most probable small fluctuation observed in phase \mathcal{A} corresponds to the phase that has the lower surface tension with \mathcal{A} , for any ordering of the chemical potentials μ_A , μ_B , and μ_C . This statement is always true when $\Delta\mu_{CB} < 0$ and is true for $\Delta\mu_{CB} > 0$ when $n_c > 1$. When $\sigma_{AB} < \sigma_{AC}$, these conditions are equivalent to the condition,

$$\Delta\mu_{CB} < \phi(\sigma_{AC} - \sigma_{AB}), \quad (3)$$

which is satisfied over a wide range of thermodynamic states in a three-phase system. Equation (3) is always satisfied when \mathcal{B} is more stable than \mathcal{C} (i.e., $\Delta\mu_{CB} < 0$), where $G_{AB} < G_{AC}$ for all n and n_c is undefined. In the region of the phase diagram where \mathcal{C} is more stable than \mathcal{B} (i.e., $\Delta\mu_{CB} > 0$), Eq. (3) is satisfied in a band of states delimited by two boundaries. The first boundary corresponds to the \mathcal{BC} coexistence line, where $\Delta\mu_{CB} = 0$ and n_c diverges. The second boundary is given by $\Delta\mu_{CB} = \phi(\sigma_{AC} - \sigma_{AB})$, beyond which $n_c < 1$. Between these two boundaries, the FPT will occur at an observable and well-defined value of $n_c > 1$. Equation (3) is thus satisfied in a region on both sides of the \mathcal{BC} coexistence line. This region necessarily encompasses the triple point of a three phase system, where complex nucleation phenomena, such as TSN, are commonly observed.

Our analysis thus predicts that whenever Eq. (3) is satisfied (e.g., near a triple point) the initial fluctuations of a bulk phase favor the local structure that has the lowest surface tension, regardless of whether or not other structures have a lower bulk chemical potential. In addition, our analysis does not depend on the value of μ_A and thus applies to the behavior of the fluctuations of \mathcal{A} regardless of whether \mathcal{A} is stable or metastable with respect to either or both of the bulk \mathcal{B} and \mathcal{C} phases. Thus in Fig. 1(e) a FPT occurs in the fluctuations of the stable \mathcal{A} phase, while in Figs. 1(d) and 1(f), a FPT occurs in the fluctuations of the metastable \mathcal{A} phase. In these two latter cases, a nucleation process from \mathcal{A} to \mathcal{C} occurs in concert with a FPT from \mathcal{B} to \mathcal{C} . The cases in Figs. 1(d) and 1(f) may thus be expected to correspond to TSN.

III. LATTICE MODEL SIMULATIONS

Next we present results obtained from a lattice model to test and elaborate on the predictions of Sec. II. As shown below, this model provides a simple example of a system having a triple point at which three distinct bulk phases coexist. Furthermore, within any one phase, fluctuations corresponding to the other two phases are easily identified.

We conduct Monte Carlo (MC) simulations of a 2D Ising model, with nearest-neighbor (nn) and next-nearest-neighbor (nnn) interactions, on a square lattice of $N = L^2$ sites with

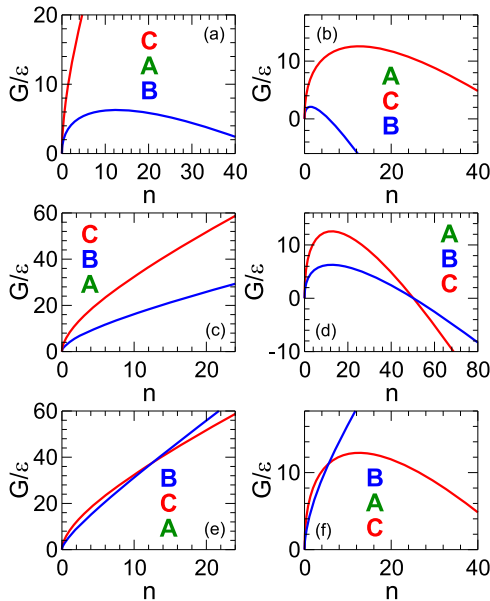


FIG. 1: G_{AB} (blue) and G_{AC} (red) versus n for $D = 2$ in various thermodynamic regimes. To plot these curves, we scale energies by $\epsilon = |\Delta\mu_{AC}|$ and surface tensions by $\epsilon v^{-\alpha}$. In all panels, $\sigma_{AC} = 2\sigma_{AB} = 2\epsilon v^{-\alpha}$. In the left-hand side panels, $\Delta\mu_{AC} = \epsilon$, and in the right-hand side panels $\Delta\mu_{AC} = -\epsilon$. From top to bottom within each column, $\Delta\mu_{AB}$ increases: (a) $\Delta\mu_{AB} = -\epsilon/2$, (b) $\Delta\mu_{AB} = -3\epsilon/2$, (c) $\Delta\mu_{AB} = \epsilon/2$, (d) $\Delta\mu_{AB} = -\epsilon/2$, (e) $\Delta\mu_{AB} = 2\epsilon$, (f) $\Delta\mu_{AB} = \epsilon/2$. To indicate the relative stability of the three bulk phases in each panel, the phases are listed vertically according to their value of μ , with μ increasing from bottom to top in each list.

periodic boundary conditions. Each site i is assigned an Ising spin $s_i = \pm 1$. The energy E of a microstate is given by

$$\frac{E}{J} = \sum_{\langle nn \rangle} s_i s_j - \frac{1}{2} \sum_{\langle nnn \rangle} s_i s_j - H \sum_{i=1}^N s_i - H_s \sum_{i=1}^N \sigma_i s_i, \quad (4)$$

where J is the magnitude of the nn interaction energy. Interactions between nn sites are antiferromagnetic, while nnn interactions are ferromagnetic. The first (second) sum in Eq. (4) is carried out over all distinct nn (nnn) pairs of sites i and j . The third and fourth terms in Eq. (4) specify the influence of the direct magnetic field H and the staggered field H_s . We define $\sigma_i = (-1)^{x_i+y_i}$, where x_i and y_i are integer horizontal and vertical coordinates of site i so that the sign of $H_s \sigma_i$ alternates in a checkerboard fashion on the lattice. We sample configurations using Metropolis single-spin-flip MC dynamics.⁴³

This model has been studied previously to model metamagnetic systems exhibiting a tricritical point, for which it provides a prototypical example in 2D.^{44–48} At $T = 0$, four stable phases are observed, depending on the values of H and H_s . We label these phases so as to maintain the “ ABC ” notation used in Sec. II. There are two ferromagnetic phases which we label B (all $s_i = 1$) and \bar{B} (all $s_i = -1$) and two antiferromagnetic phases labelled C (all $s_i = \sigma_i$) and A (all $s_i = -\sigma_i$). Since the topology of the phase diagram is unchanged when $H \rightarrow -H$, we only consider $H > 0$ here. Consequently the \bar{B} phase will not appear in our analysis. All our simulations are carried out at temperature T such that $\beta J = 1$, where $\beta = 1/kT$ and k is Boltzmann’s constant. This is well below T for the Néel transition ($kT/J = 3.802$) and the tricritical point ($kT/J = 1.205$).⁴⁶ Thus the phase diagram in the plane of H and H_s at fixed $kT/J = 1$ contains only first-order phase transitions, arranged as three coexistence lines meeting at a triple point located at $H_s = 0$ and $H = 3.9876$, as shown in Fig. 2. See Secs. S1–S3 of the supplementary material and Refs. 43, and 49–51 for the details of our phase diagram calculation.

The phase diagram presented in Fig. 2 also includes the metastable extensions of the AC , BC , and AB coexistence lines. The phase diagram is thereby divided into six distinct regions each corresponding to a unique ordering of the chemical potentials μ_A , μ_B , and μ_C . Furthermore, as shown in Sec. S4 of the supplementary material, we find that $\sigma_{AB} < \sigma_{AC}$ throughout the region of the (H_s, H) plane explored here.^{50,52–54} Our lattice model thus realizes the relationships between the surface tensions and chemical potentials considered in Sec. II: The six regions of the phase diagram in Fig. 2 correspond to the six panels of Fig. 1. If we choose the A phase of the lattice model to correspond to the A phase of Sec. II, then the predictions of Sec. II can be tested by examining the behavior of the fluctuations of A in the lattice model in the various regions of the model phase diagram.

To explore the scenarios predicted in Sec. II, we must characterize the fluctuations that appear in the bulk A phase. Due to the simplicity of our lattice model, we show in Sec. S5 of the supplementary material that it is straightforward to identify all local fluctuations as clusters of size n that deviate from the structure of A . All sites within a given cluster can further

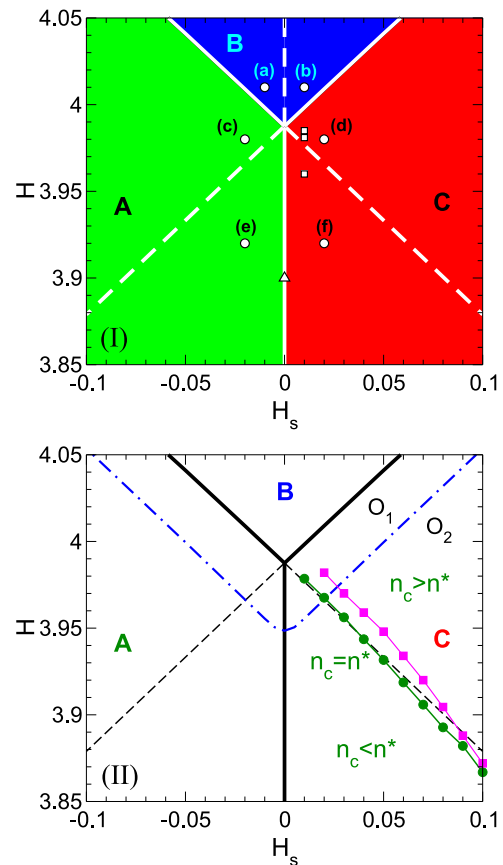


FIG. 2. Phase diagram for $kT/J = 1$. Solid lines are coexistence lines and dashed lines are metastable extensions of coexistence lines. In panel (I), the stability field of each phase is indicated with a solid color, green for A , blue for B , and red for C . The six regions demarcated by the solid and dashed lines are labelled (a)–(f) and correspond to the six identically labelled cases shown in Fig. 1. The triangle locates the state studied in Sec. IV. Squares locate the three states studied in Sec. V. Circles locate the six states for which the nucleation barriers are presented in Fig. 14. In panel (II), the dotted-dashed line is the limit of metastability (LOM) of the bulk B phase for a system of size $L = 64$. Green circles locate points on the line \mathcal{L}_n at which $n_c = n^*$. Magenta squares locate points on the line at which $\beta G^* = 20$; below this line $\beta G^* > 20$ and above it, $\beta G^* < 20$. O_1 labels the region bounded by the AB and BC coexistence lines and the LOM of the B phase. O_2 labels the region between the AB and BC coexistence lines and which lies beyond the LOM of the B phase.

be classified according to their correspondence to either B or C . We thereby define the phase composition of each cluster as $f = \bar{n}/n$, where \bar{n} is the number of sites in the cluster that are classified as C . Figure 3 shows example clusters of various n and f , from mostly B -like ($f \rightarrow 0$) to mostly C -like ($f \rightarrow 1$).

To quantify the thermodynamic behavior of the fluctuations that occur in A , we measure $G(n_{\max}, f)$, the FES of the bulk A phase in which the largest non- A cluster in the system is of size n_{\max} and has composition f .¹⁷ We obtain the FES from umbrella sampling MC simulations at fixed (N, H_s, H, T) .⁵¹ We compute $G(n_{\max}, f)$ from

$$\beta G(n_{\max}, f) = -\log[P(n_{\max}, f)] + C, \quad (5)$$

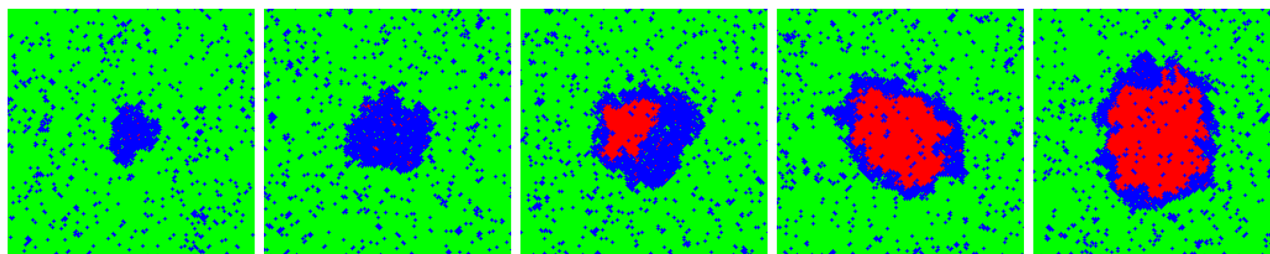


FIG. 3. System configurations containing fluctuations of different sizes and compositions obtained from 2D umbrella sampling simulations carried out at $H_s = 0.01$, $H = 3.981$, and $L = 200$. As described in Sec. S5 of the [supplementary material](#), green sites have a local structure corresponding to the \mathcal{A} phase, blue to the \mathcal{B} phase, and red to the \mathcal{C} phase. From left to right, $(n_{\max}, f) = (1393, 0.020)$, $(3476, 0.040)$, $(5474, 0.303)$, $(7492, 0.583)$, and $(9658, 0.633)$. This sequence of microstates approximately follows the path of $\langle f \rangle$ shown in [Fig. 8\(b\)](#) and illustrates the two-step nature of the nucleation process under these conditions.

where $P(n_{\max}, f)$ is proportional to the probability to observe a microstate with values n_{\max} and f . The value of the arbitrary constant C is chosen so that the global minimum of $G(n_{\max}, f)$ is zero. We estimate $P(n_{\max}, f)$ from 2D umbrella sampling simulations using a biasing potential that depends on both n_{\max} and f ,

$$U_B = \kappa_n (n_{\max} - n_{\max}^*)^2 + \kappa_f (f - f^*)^2, \quad (6)$$

where n_{\max}^* and f^* are the target values of n_{\max} and f to be sampled in a given umbrella sampling simulation and κ_n and κ_f control the range of sampling around n_{\max}^* and f^* . See Sec. S6 of the [supplementary material](#) for details of our 2D umbrella sampling simulations. Results from multiple umbrella sampling runs conducted at fixed (N, H_s, H, T) are combined using the weighted histogram analysis method (WHAM) to estimate the full $G(n_{\max}, f)$ FES at a given state point.^{51,55,56} Once $G(n_{\max}, f)$ has been calculated, we can also compute the one dimensional (1D) free energy as a function of n_{\max} alone, defined as

$$\beta G_1(n_{\max}) = -\log \int_0^1 \exp[-\beta G(n_{\max}, f)] df. \quad (7)$$

In addition to the 2D umbrella sampling simulations described above, we also conduct 1D umbrella sampling simulations in which n_{\max} alone is constrained. In this approach, we directly compute $G_1(n_{\max})$ using

$$\beta G_1(n_{\max}) = -\log[P_1(n_{\max})] + C, \quad (8)$$

where $P_1(n_{\max})$ is proportional to the probability to observe a microstate with a given value of n_{\max} and C is chosen so that the global minimum of $G_1(n_{\max})$ is zero. The details of our 1D umbrella sampling runs are given in Sec. S7 of the [supplementary material](#). We obtain the size of the critical nucleus n^* from the value of n_{\max} at the maximum of $G_1(n_{\max})$.

Although the maximum in $G_1(n_{\max})$ properly identifies n^* , it is important to note that the height of the maximum in $G_1(n_{\max})$ does not correspond to the nucleation barrier described by CNT. The nucleation barrier is more accurately estimated by computing,

$$\beta \bar{G}(n) = -\log \frac{\mathcal{N}(n)}{N}, \quad (9)$$

where $\mathcal{N}(n)$ is the average number of clusters of size n in a system of size N .⁵⁷⁻⁵⁹ The height of the nucleation barrier is then defined as $G^* = \bar{G}(n^*)$. Since we also evaluate $\mathcal{N}(n)$ from our 1D umbrella sampling simulations, we are able to estimate $\bar{G}(n)$ and G^* for these cases. Examples of our calculations of $\bar{G}(n)$ are given in Sec. S8 of the [supplementary material](#).

IV. FLUCTUATION PHASE TRANSITION IN A STABLE PHASE

In this section, we analyze the behavior observed in the fluctuations of \mathcal{A} when \mathcal{A} is stable and no nucleation process is possible. As an example, we focus on the state point $(H_s, H) = (0, 3.9)$. This point is on the \mathcal{AC} coexistence line, and so the nucleation barrier to convert \mathcal{A} to \mathcal{C} is infinitely large. In terms of the analysis of Sec. II, this point is on the boundary of the regions described by panels (e) and (f) of [Fig. 1](#). We thus expect that the fluctuations of \mathcal{A} are \mathcal{B} -like at small n_{\max} and then undergo a FPT to \mathcal{C} at n_c .

We present the FES describing the fluctuations of \mathcal{A} at this state point in [Fig. 4](#). Under these conditions, all local fluctuations that induce a deviation from the most probable state of the \mathcal{A} phase increase the system free energy, regardless of their size or composition. The FES therefore exhibits only one basin with a minimum in the lower-left corner of [Fig. 4\(b\)](#) associated with the bulk \mathcal{A} phase, and no transition states (i.e., saddle points) occur on the surface. However, the FES is not featureless. It contains two channels, indicated by the red and blue lines in [Fig. 4\(b\)](#). These lines locate the values of f at which a local minimum occurs in $G(n_{\max}, f)$ at a fixed value of n_{\max} . Along the low- f channel, \mathcal{B} fluctuations dominate, while the high- f channel corresponds to fluctuations in which the core is \mathcal{C} , wetted by a surface layer of \mathcal{B} . We define f_B as the values of f along the minimum of the low- f channel and f_C for the high- f channel.

It is notable that the two channels are unconnected and that neither channel is defined for all n_{\max} . At small n_{\max} , only the \mathcal{B} channel exists, while only the \mathcal{C} channel exists at large n_{\max} . This behavior is highlighted in [Fig. 5](#), where we show cuts through the FES at fixed n_{\max} . For a finite range of n_{\max} , G versus f exhibits two minima with a maximum in between. At

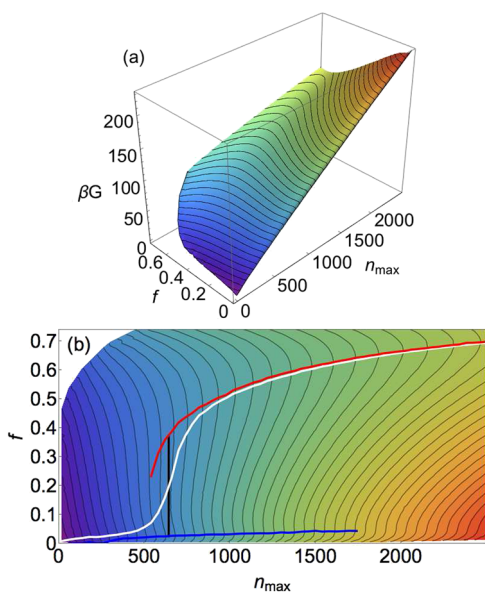


FIG. 4. (a) Surface plot and (b) contour plot of $G(n_{\max}, f)$ for $(H_s, H) = (0, 3.9)$ and $L = 128$. Contours are $5kT$ apart in both (a) and (b). In (b), we also plot f_B (blue line), f_C (red line), and $\langle f \rangle$ (white line). The black vertical line is located at $n_{\max} = n_c$.

small n_{\max} , the high- f minimum disappears, and at large n_{\max} , the low- f minimum disappears.

To quantify the relative free energies associated with these two channels, we define, for a fixed value of n_{\max} ,

$$\begin{aligned} \beta G_B &= -\log \int_0^{f_{\max}} \exp[-\beta G(n_{\max}, f)] df, \\ \beta G_C &= -\log \int_{f_{\max}}^1 \exp[-\beta G(n_{\max}, f)] df, \end{aligned} \quad (10)$$

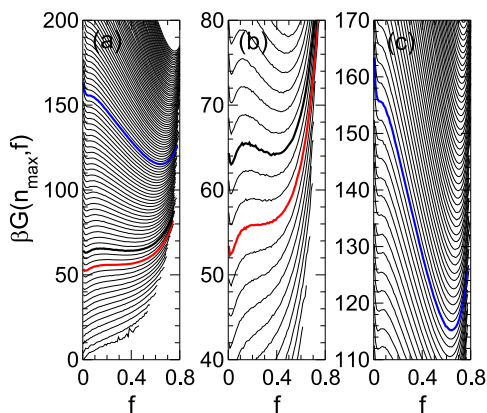


FIG. 5. Cuts through the $G(n_{\max}, f)$ surface at fixed n_{\max} for $(H_s, H) = (0, 3.9)$ and $L = 128$. n_{\max} changes by 40 from one cut to the next. Several cuts are highlighted: The red curve is for $n_{\max} = 539$ and corresponds to the spinodal endpoint of the C channel. The blue curve is for $n_{\max} = 1739$ and corresponds to the spinodal endpoint of the B channel. The thick black curve is for $n_{\max} = 659$ and corresponds to the point of coexistence between the B and C channels at $n_{\max} = n_c$.

where f_{\max} is the value of f at which a local maximum occurs in $G(n_{\max}, f)$ as a function of f at fixed n_{\max} if the maximum exists. If f_B is defined but f_C is not, then f_{\max} is set to 1. If f_C is defined but f_B is not, then f_{\max} is set to 0. So defined G_B and G_C decompose G_1 into contributions associated with the respective B and C channels.

We plot G_B , G_C , and G_1 in Fig. 6. We see that the B channel makes the dominant contribution to the total free energy at small n_{\max} , while the C channel dominates at large n_{\max} . A well-defined FPT is identified by the intersection of G_B and G_C and corresponds to a “kink” in the G_1 curve. The value of n_{\max} at this intersection defines n_c and identifies the coexistence condition where distinct B -dominated and C -dominated fluctuations of equal size are equally probable. We further see that both the channels have metastable extensions beyond n_c that end at well-defined limits of metastability (LOM), occurring at the values of n_{\max} where the low- f and high- f minima disappear, as highlighted in Fig. 5. In the following, we use the term “spinodal” to refer to the limit of metastability that terminates a channel in the FES, in analogy to the use of this term when referring to the limit of metastability of a bulk phase in a mean-field system. The behavior shown in Fig. 6, where both coexistence and metastability are observed, demonstrates that the FPT is a first-order phase transition occurring in a finite-sized system (the fluctuation) as the system size (n_{\max}) increases.

An appropriate order parameter for the FPT is f . For a fixed value of n_{\max} , we define

$$\langle f \rangle = \frac{\int_0^1 f \exp[-\beta G(n_{\max}, f)] df}{\int_0^1 \exp[-\beta G(n_{\max}, f)] df}. \quad (11)$$

We plot $\langle f \rangle$ in Fig. 4(a). The variation of $\langle f \rangle$ is steepest at $n_{\max} = n_c$. Even though the FPT is first-order, $\langle f \rangle$ does not jump discontinuously at n_c because of the finite size of the system. However, the most probable value of f does have a jump discontinuity at n_c . We also note that the fluctuations of f at fixed

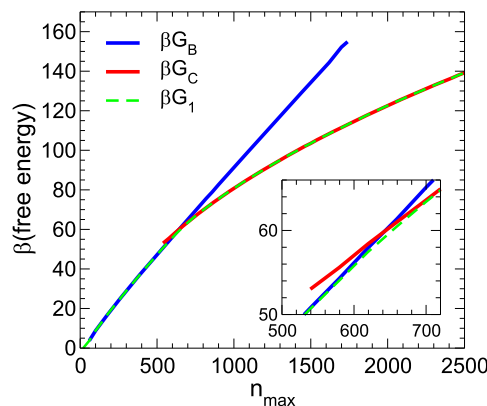


FIG. 6. G_B , G_C , and G_1 for $(H_s, H) = (0, 3.9)$ and $L = 128$. The inset shows a closeup of the same data as in the main panel highlighting the intersection of G_B and G_C at $n_{\max} = n_c$.

n_{\max} can be defined as

$$\chi = \langle f^2 \rangle - \langle f \rangle^2. \quad (12)$$

As shown in Sec. S9 of the [supplementary material](#), n_c can be accurately estimated as the value of n_{\max} at which a maximum occurs in χ . This procedure allows n_c to be evaluated without having to separately compute G_B and G_C .

The spinodal endpoints that terminate the G_B and G_C curves are a significant difference between the behavior plotted in Fig. 6 and that predicted in Fig. 1(e). In our lattice model, a thermodynamic distinction between the B and C fluctuations only exists for n_{\max} between these spinodals, where both channels are observed. These spinodals have important physical consequences. At small n_{\max} , the most probable fluctuations are always B -like; C -like fluctuations, although they may occur, have no local stability relative to changes in f . This occurs in spite of the fact that C has a lower bulk-phase chemical potential than B under these conditions. Thus the prediction made in Sec. II, that the most probable small fluctuation corresponds to the phase with the lowest surface tension, becomes even stronger in our lattice model: Not only is this small fluctuation most probable but also it is the *only* fluctuation that is stable with respect to changes in composition. This observation is in line with a similar conclusion obtained by Harrowell, who predicted that sub-critical clusters in a supercooled liquid are not stable as crystal-like clusters below a threshold size.⁶⁰ The same is true here for our C fluctuations.

Conversely, at sufficiently large n_{\max} , only C fluctuations are stable with respect to changes in composition. That is, even though a fluctuation is most likely to start out as a B fluctuation and even if it persists as a B fluctuation in the metastable portion of the B channel when $n_{\max} > n_c$, it cannot remain a B fluctuation at arbitrarily large n_{\max} . It must eventually convert to C .

Most of the features of the FES discussed here, including the FPT, occur for $G \gg kT$. As a consequence, the most commonly observed fluctuations of \mathcal{A} are entirely dominated by B , despite the lower bulk chemical potential of C . Nonetheless, observable effects associated with the FPT can be observed in this system during non-equilibrium processes. For example, consider the case in which a large cluster of the C phase is inserted into the bulk \mathcal{A} phase under the conditions corresponding to the FES in Fig. 4 so that the system starts out close to the C channel at large f and large n_{\max} . If this non-equilibrium system is then allowed to evolve unconstrained, the C cluster will spontaneously shrink in size and the system point will flow “downhill” along the C channel of the FES. So long as the degrees of freedom associated with changes in f relax quickly relative to the rate at which the cluster size decreases, the shrinking cluster will then undergo a FPT from C to B at some size between n_c and the spinodal of the C channel. The B cluster so formed will then spontaneously shrink and disappear as the system approaches equilibrium in the lower left-hand corner of the FES. On the other hand, if a large cluster of the B phase is inserted into the bulk \mathcal{A} phase under the same conditions so that the system starts out on the B channel at low f , the system evolution will follow the

B channel downhill towards equilibrium. In this case, the B cluster will simply shrink and disappear and no FPT will be observed.

These examples illustrate the differences between the FPT described here and a conventional first-order phase transition occurring between bulk phases. The FPT occurs in a finite-sized system (the fluctuation), which arises as a departure from the most probable state of the surrounding system (the homogeneous bulk phase). In a bulk phase transition, the parameter that drives the system through the phase transition is usually an externally imposed quantity, such as temperature or pressure. However, as in the examples above, the parameter that drives the fluctuation through the FPT is the size of the fluctuation itself. The size of a fluctuation will normally be subject to strong thermodynamic driving forces that cause it to spontaneously increase or decrease in size. The dynamics of the system and its preparation history will therefore have a significant influence on if and how a FPT is observed in a particular case.

V. TWO-STEP NUCLEATION: FLUCTUATION PHASE TRANSITION IN A METASTABLE PHASE

We now focus on state points where \mathcal{A} is metastable and C is stable, i.e., regions (d) and (f) in the phase diagram of Fig. 2. Based on the predictions of Sec. II, we expect in regions (d) and (f) that small B fluctuations appear first and then convert to C at larger size via a FPT, just like in region (e). However, in regions (d) and (f), we should also observe a transition state in the FES that is absent in region (e). For n_{\max} beyond this transition state, the fluctuation will grow in size spontaneously, leading ultimately to the formation of the bulk C phase. In this case, C is formed from \mathcal{A} via a TSN process, in which the B fluctuations that occur initially play the role of the intermediate phase.

Figures 7 and 8 show the FES at fixed $H_s = 0.01$ for three values of H within the stability field of C . G_1 , G_B , and G_C are shown for each of these cases in Fig. 9. In Sec. S10 of the [supplementary material](#), we provide additional plots of the FES for other values of H between 3.960 and 3.985. The free energy basin in the lower left corner of each surface in Fig. 8 now corresponds to the metastable bulk \mathcal{A} phase, and the channel in the upper right corner leads to the stable C phase. In all cases, we observe a FPT with the same set of features found when \mathcal{A} is stable: There are two distinct, unconnected channels in the FES. As shown in Fig. 9, the coexistence value of n_c is well defined at the crossing of G_B and G_C and is coincident with a kink in G_1 . The variation of $\langle f \rangle$ with n_{\max} is steepest in the vicinity of n_c (Fig. 8). We also observe the lower spinodal limit for the C channel; the upper spinodal limit for the B channel is beyond the range of n_{\max} accessible to our simulations for this system size ($L = 200$).

In Fig. 10, we show $G(n_{\max} = n_c, f)$, the cut through the $G(n_{\max}, f)$ surface at the point of coexistence between the B and C channels, for each FES plotted in Figs. 7 and 8. We see that the height of the free energy barrier between the two channels at the coexistence condition increases with n_c . This is in line with the expectation for a first-order phase transition

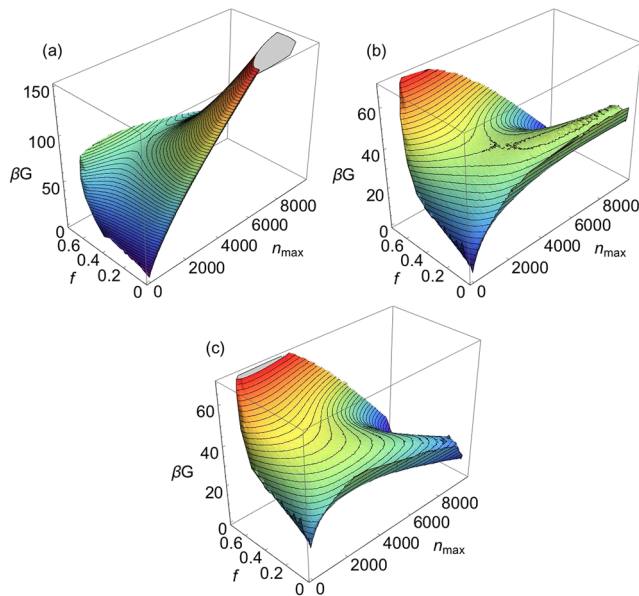


FIG. 7. Surface plots of $G(n_{\max}, f)$ for $H_s = 0.01$ and $L = 200$. Panels (a), (b), and (c) correspond to $H = \{3.96, 3.981, 3.985\}$, respectively. Contours are $2kT$ apart.

occurring in a finite-sized system (i.e., the fluctuation).^{52,53} As the size of the fluctuation increases, the phase transition within it must surmount a larger barrier because of the larger interface that must be created between the \mathcal{C} -like core and the wetting layer of \mathcal{B} that surrounds the core.

In addition to the FPT, each FES in Figs. 7 and 8 exhibits features associated with the nucleation process by which the metastable \mathcal{A} phase converts to the stable \mathcal{C} phase. Figure 9 shows that G_1 in this regime exhibits a maximum at $n_{\max} = n^*$ corresponding to the size of the critical nucleus. We also observe that the kink in G_1 corresponding to $n_{\max} = n_c$ may occur either before or after n^* . Figures 8(a) and 8(c) thus typify two distinct regimes of behavior: In Fig. 8(a), $n_c < n^*$ while in Fig. 8(c) $n_c > n^*$. We also see in Figs. 8(a) and 8(c) that the value of n^* corresponds closely to n_{\max} at which a saddle point occurs in the FES. This saddle point locates the most probable transition state at which the system exits the basin of the metastable phase. Thus the FPT can occur either before or after the transition state. We also find that all the qualitative features of the FPT occur in exactly the same way regardless of whether the FPT occurs before or after the transition state. This behavior emphasizes that the FPT is an independent phenomenon from the nucleation process.

Our results thus demonstrate that the superposition of a FPT on the nucleation process generates the characteristic signatures of TSN. When $n_c < n^*$ [Fig. 8(a)], the FPT occurs in the sub-critical nucleus. In this case, the most probable small nucleus resembles the \mathcal{B} phase and a small \mathcal{C} nucleus is unstable with respect to fluctuations in f . Then as it grows larger the most probable nucleus switches to the \mathcal{C} phase (via the FPT) prior to reaching the critical size, and so the structure of the

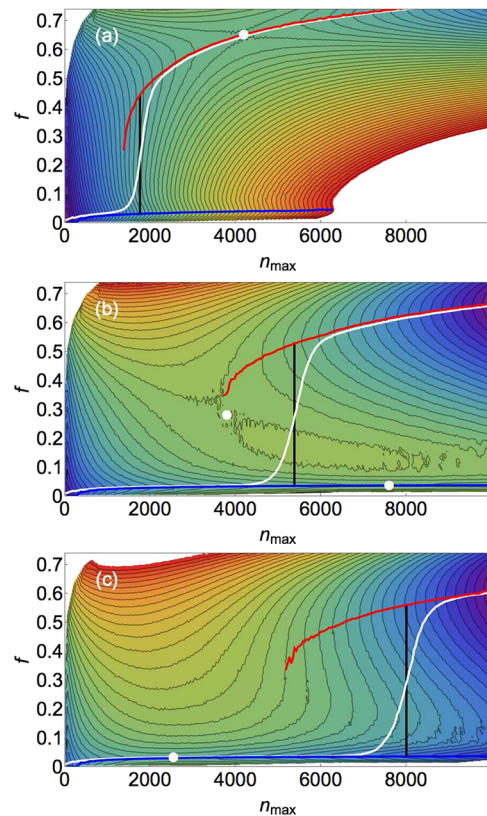


FIG. 8. Contour plots of $G(n_{\max}, f)$ for $H_s = 0.01$ and $L = 200$. Panels (a), (b), and (c) correspond to $H = \{3.96, 3.981, 3.985\}$, respectively. Contours are $2kT$ apart. In each panel, we also plot f_B (blue line), f_C (red line), and f (white line). The black vertical line is located at $n_{\max} = n_c$. The white dots locate saddle points in the FES.

critical nucleus reflects the structure of the bulk stable phase that will ultimately form.

When $n_c > n^*$ [Fig. 8(c)], the FPT occurs in the post-critical nucleus. In this regime, the most probable nucleus resembles the \mathcal{B} phase all the way up to and beyond the size of the critical nucleus. Indeed, in Fig. 8(c), we see that a \mathcal{C} nucleus is unstable at n^* . As a consequence, the structure of the most probable critical nucleus bears no resemblance to the stable \mathcal{C} phase, and cannot do so, even as a metastable nucleus. The post-critical \mathcal{B} nucleus then grows spontaneously along the \mathcal{B} channel in the FES. The transition of this growing post-critical \mathcal{B} nucleus to the \mathcal{C} channel only becomes thermodynamically possible for n_{\max} greater than that of the lower spinodal for the \mathcal{C} channel and is only likely to occur for $n_{\max} \geq n_c$. These observations emphasize that the transition state (saddle point) is not necessarily the entrance to the basin of the stable phase. Rather, it only identifies the exit from the basin of the metastable phase.

The topology of the FES in Fig. 8(c) exposes the difference between the first and second “steps” of TSN when $n_c > n^*$. The first step is a conventional barrier-crossing process where the transition state corresponds to a well-defined

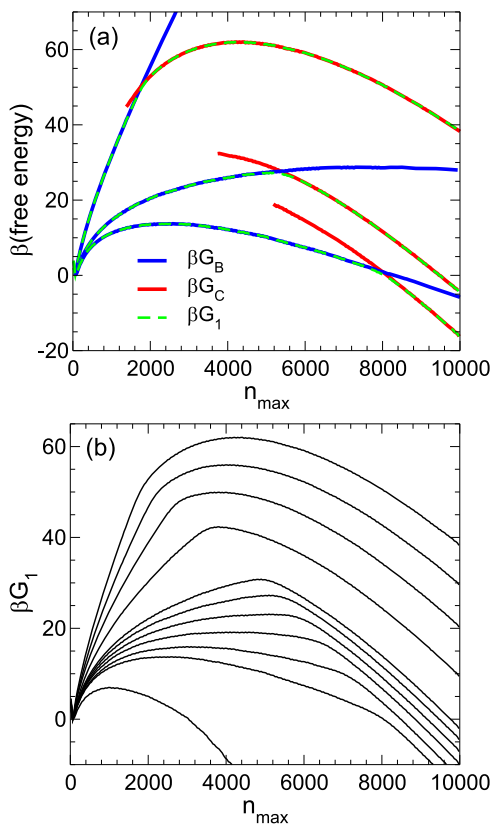


FIG. 9. (a) G_B , G_C , and G_1 for $H_s = 0.01$ and $L = 200$. From top to bottom, $H = \{3.96, 3.981, 3.985\}$. (b) G_1 for $H_s = 0.01$ and $L = 200$. From top to bottom $H = \{3.960, 3.965, 3.970, 3.975, 3.980, 3.981, 3.982, 3.983, 3.984, 3.985, 3.990\}$.

saddle point. The size and composition of the critical nucleus at this step are defined solely by the thermodynamic features encoded in the FES. The second step is associated with the

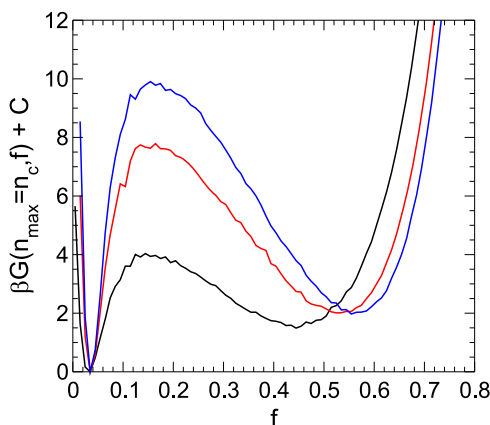


FIG. 10. $G(n_{\max} = n_c, f)$ for $H_s = 0.01$ and $L = 200$. The black curve corresponds to $H = 3.96$ and $n_{\max} = 1779$. The red curve corresponds to $H = 3.981$ and $n_{\max} = 5379$. The blue curve corresponds to $H = 3.985$ and $n_{\max} = 8019$. Each curve has been shifted by a constant C so that the minimum value is zero.

FPT and is a process where the system does not pass through a saddle point but rather crosses over an extended ridge in the FES.²¹ Consequently, even though n_c is defined by the properties of the FES, the average size of the post-critical nucleus when it crosses the ridge may not be determined solely by the FES. For example, if the degrees of freedom associated with changes in f relax much faster than those associated with changes in the size of the nucleus, then we can expect the FPT to occur close to n_c . In this case, the average path of the system on the FES will follow closely the curve for $\langle f \rangle$. However, if the relaxation of f is comparable to or slower than for n_{\max} , then it is likely that the growing nucleus will significantly “overshoot” the coexistence condition at n_c and continue to grow in size along the (now metastable) \mathcal{B} channel. In this case, the average path of the system on the FES will not follow $\langle f \rangle$. Thus when $n_c > n^*$, the second step of TSN is qualitatively different from the first: The nucleation pathway for the first step is entirely controlled by thermodynamics, whereas the pathway for the second step depends on both thermodynamic and dynamic factors. This distinction can help explain the wide variety of behavior observed in TSN in different systems.

Figure 8(b) corresponds to the case when $n_c \sim n^*$ and displays complex behavior. We observe two saddle points on either side of an unusually flat region of the FES. Although n_c and n^* are close in value, n^* is not close to the value of n_{\max} of either saddle point. In this case, the transition state in the FES by which the system leaves the metastable state is not sharply defined. As a consequence, we can expect particularly strong deviations from CNT in this regime.

An example of the unusual behavior occurring when $n_c \sim n^*$ is shown in Fig. 11, where we plot n_c and n^* as a function of H at fixed $H_s = 0.01$. As shown in Fig. 9, the height of the nucleation barrier decreases monotonically as H increases. However, in Fig. 11, we observe that n^* does not decrease monotonically with H but rather exhibits a minimum and a maximum in the vicinity of the value of H at which $n_c = n^*$.

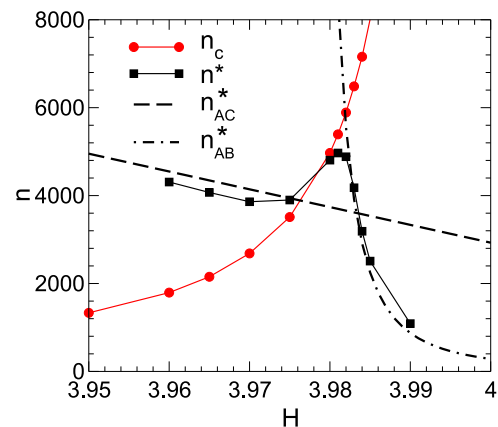


FIG. 11. Plot of n_c and n^* versus H , for $H_s = 0.01$ and $L = 200$ as obtained from our 2D umbrella sampling simulations. Also shown are the CNT predictions for n_{AC}^* and n_{AB}^* computed as described in the text.

This complex and highly non-classical behavior arises from the crossover from the $n_c < n^*$ to the $n_c > n^*$ regime as H increases. To understand this effect, we consider the CNT expression^{6,7} for n^* in $D = 2$, $n^* = \pi\sigma^2/(\Delta\mu)^2$. As described in the [supplementary material](#), we have obtained approximate expressions to describe the dependence on H and H_s of the chemical potentials (see Sec. S3 of the [supplementary material](#)) and surface tensions (see Sec. S4 of the [supplementary material](#)) for all three phases in our lattice model. We use these expressions to calculate the CNT prediction for the variation of n^* with H and compare this with the observed behavior. In [Fig. 11](#), we show that for $n_c < n^*$, the H -dependence of n^* approximately follows that expected for the nucleation of \mathcal{C} directly from \mathcal{A} , $n_{AC}^* = \pi\sigma_{AC}^2/(\Delta\mu_{AC})^2$. While $\Delta\mu_{AC}$ is constant for all H at fixed H_s , n_{AC}^* decreases gradually with H due to the approximately linear decrease of σ_{AC}^2 with H . However, when $n_c > n^*$, the H -dependence of n^* switches to follow the prediction for the nucleation of \mathcal{B} directly from \mathcal{A} , $n_{AB}^* = \pi\sigma_{AB}^2/(\Delta\mu_{AB})^2$. In this expression, σ_{AB} is constant with H , but the magnitude of $\Delta\mu_{AB}$ increases linearly as H increases at fixed H_s , resulting in a fast decrease of n^* . The crossover in the behavior of n^* occurs when the barrier for the $\mathcal{A} \rightarrow \mathcal{B}$ process becomes smaller than that for the $\mathcal{A} \rightarrow \mathcal{C}$ process. Interestingly, at the point of this crossover, the critical nucleus along the \mathcal{B} channel is larger than that on the \mathcal{C} channel, resulting in the maximum in n^* observed in [Fig. 11](#).

VI. TWO-STEP NUCLEATION AND BULK PHASE BEHAVIOR

We next seek to identify where in the phase diagram the different regimes of TSN occur. To do so, we quantify the variation of n_c and n^* over a wide range of H and H_s within the stability fields of \mathcal{A} and \mathcal{C} . We achieve this efficiently by augmenting the results obtained from our 2D umbrella sampling runs with 1D umbrella sampling simulations, as described in Sec. S7 of the [supplementary material](#). As shown in [Fig. 12\(a\)](#), we find that the variation of n_c with H and H_s is relatively simple: For fixed H_s , n_c grows and diverges as H approaches the \mathcal{BC} coexistence line \mathcal{L}_{BC} from below. This behavior is anticipated by the form of Eq. (2) and confirmed in [Fig. 13](#), where we plot n_c as a function of $\Delta\mu_{CB}$ for various values of H_s , both positive and negative. The data for all values of H_s fall on a single master curve. [Figure 13](#) confirms the prediction of Eq. (2) that n_c diverges as $\Delta\mu_{CB} \rightarrow 0$ (i.e., approaching \mathcal{L}_{BC}) and does not depend on μ_A , which changes as H_s changes. That is, the value of n_c is unaffected by the presence or absence of a nucleation process and is an intrinsic property of the fluctuations of \mathcal{A} .

The variation of n^* for various H_s is shown in [Fig. 12\(b\)](#). We find that the maximum of n^* noted in [Fig. 11](#) is sharpest at small H_s and fades in prominence as H_s increases. For each H_s , we locate the intersection of n_c and n^* and plot the locus of points \mathcal{L}_n at which $n_c = n^*$ in [Fig. 2](#). For H less than \mathcal{L}_n , TSN will be observed where $n_c < n^*$; for H greater than \mathcal{L}_n , TSN with $n_c > n^*$ will occur.

Notably, we find that \mathcal{L}_n is nearly coincident with the \mathcal{AB} coexistence line \mathcal{L}_{AB} , especially as $H_s \rightarrow 0$. This

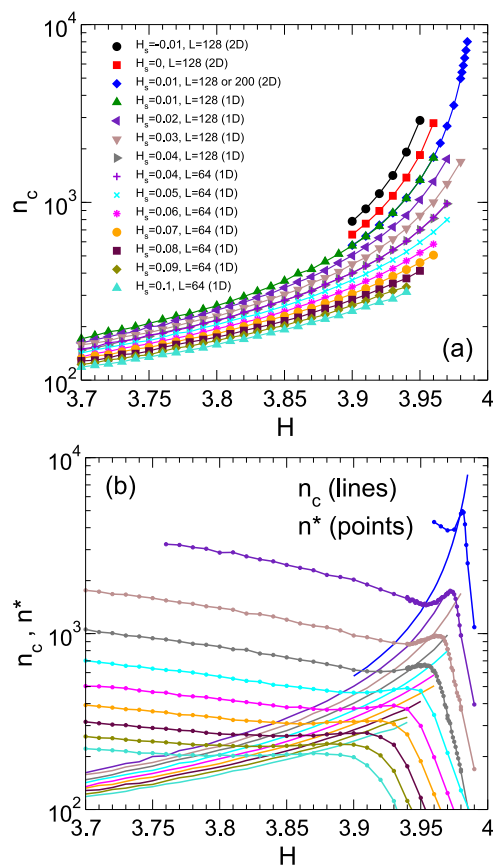


FIG. 12. (a) n_c versus H for various H_s . Data are obtained from either 1D or 2D umbrella sampling simulations, as indicated in the legend. For data obtained from 2D umbrella sampling runs at $H_s = 0.01$, we use a system of size $L = 128$ for $H < 3.96$ and $L = 200$ for $H \geq 3.96$. (b) Lines without symbols plot n_c versus H , for H_s from 0.01 to 0.10 in steps of 0.01, from top to bottom. Lines with dots plot our data for n^* versus H , for the same set of H_s values, from top to bottom. Data for n^* at $H_s = 0.01$ are obtained from 2D umbrella sampling runs with $L = 200$. Data for n^* at $H_s = \{0.02, 0.03, 0.04\}$ are obtained from 1D umbrella sampling runs with $L = 128$. All other n^* data are obtained from 1D umbrella sampling runs with $L = 64$.

correspondence occurs in our model due to a combination of influences. Based on Eq. (1), we would expect that \mathcal{L}_n should occur for H above \mathcal{L}_{AB} since $\Delta\mu_{AB} < 0$ is required to form a \mathcal{B} -like nucleus that grows spontaneously within \mathcal{A} . However, [Fig. 11](#) shows that the intersection of n_c and n^* occurs at lower H than predicted by our simple CNT analysis due to the complexity of the FES when $n_c \sim n^*$. In addition, we see in [Fig. 12\(b\)](#) that n^* drops very quickly for H above \mathcal{L}_n . Related to this behavior, we also observe that the height of the nucleation barrier G^* decreases rapidly for H above \mathcal{L}_n . See Sec. S8 of the [supplementary material](#) for an example of our calculation of G^* .^{57–59} In [Fig. 2](#), we plot the locus along which $\beta G^* = 20$, which we find lies close to and just above \mathcal{L}_n . For H above the $\beta G^* = 20$ locus, the basin of metastability for \mathcal{A} quickly becomes poorly defined and the TSN process consists of an almost barrierless decay to a spontaneously growing

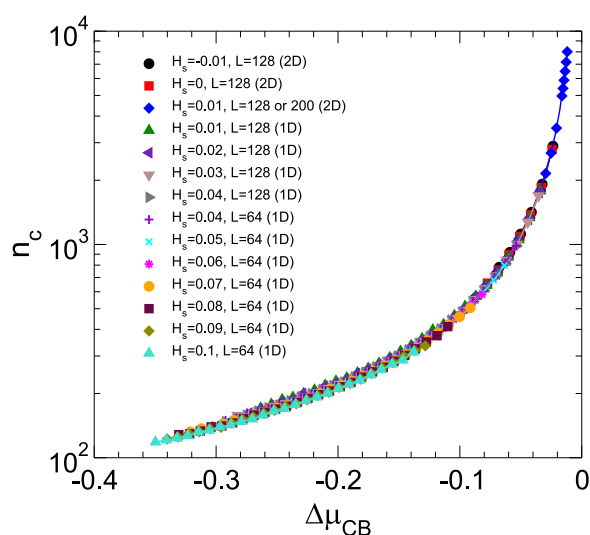


FIG. 13. Same data as in Fig. 12(a) but plotted versus $\Delta\mu_{CB}$ instead of H .

nucleus of \mathcal{B} , which eventually converts to \mathcal{C} via the FPT. As a result of these effects, \mathcal{L}_n is on the one hand unlikely to occur much below \mathcal{L}_{AB} and on the other hand is unlikely to occur much above it. These factors effectively constrain \mathcal{L}_n to lie very close to \mathcal{L}_{AB} . If this behavior proves to be common in other systems, it provides a simple way to predict the crossover from the $n_c < n^*$ to the $n_c > n^*$ regime, by locating the metastable extension of the bulk phase coexistence line for the two phases involved in the FPT.

We have also assessed the limits of metastability (LOM) of the bulk \mathcal{B} phase, as described in Sec. S2 of the [supplementary material](#). In practice, the LOM of a homogeneous bulk phase depends on the system size.⁵³ For a small system, the LOM for a given bulk phase may occur significantly outside the stable phase boundary of that phase, but as $L \rightarrow \infty$, the LOM approaches the stable phase boundary. We show an example in Fig. 2(b), where we plot the LOM for the bulk \mathcal{B} phase for $L = 64$. The LOM for each of our system sizes with $L > 64$ lies between the boundary shown in Fig. 2(b) and the \mathcal{AB} and \mathcal{BC} coexistence curves. Therefore most of our results for n_c in Fig. 12 are obtained beyond the LOM of the bulk \mathcal{B} phase for the system sizes studied here, demonstrating that the FPT remains well-defined even when the bulk \mathcal{B} phase is unstable. Furthermore, small fluctuations occurring within the \mathcal{A} phase always resemble the \mathcal{B} phase, even when the bulk \mathcal{B} phase is unstable, in both the $n_c < n^*$ and the $n_c > n^*$ regimes. These observations emphasize that a local structure that is unstable as a bulk phase can still play a significant role, both as the dominant small fluctuation and as an “intermediate phase” in a TSN process.

VII. RELATIONSHIP TO PREVIOUS MODELLING OF TWO-STEP NUCLEATION

As indicated in the Introduction, a number of previous simulation and theoretical studies have examined

behavior related to TSN. Previous studies have also demonstrated that many complex nucleation phenomena can be elucidated by studying lattice models similar to the one employed here.^{17,19,20,61–67} Notably, this work reproduces several phenomena first identified by Duff and Peters¹⁷ who also used a lattice model. Their work introduced the FES in the specific form that we use and showed that the conversion of the nucleus to the stable phase can occur before or after the transition state, although in the latter case the conversion of the nucleus was not explicitly observed. Their simulations also did not allow the calculation of FES of sufficient resolution to resolve the first-order character of the FPT as observed here, and they did not identify the spinodals that bracket the FPT. Reference 17 presents a CNT-based analysis of TSN, although the implications for the nature of fluctuations in general was not explored.

The analytical study of TSN by Iwamatsu²¹ identified the thermodynamic conditions for the conversion of the nucleus to the stable phase, pointed out its first-order character, and noted that this conversion crosses a ridge in the FES. This work also showed that the FES may display two distinct saddle points, as observed here. However, Ref. 21 argued that there were cases where the FES has two independent channels leading out of the metastable phase, in contrast to our results, where we find only one. Furthermore, Ref. 21 did not identify cases in which the conversion of the nucleus to the stable phase occurs before reaching the transition state, nor did it identify spinodal endpoints along any channel in the FES. These differences may arise from fundamental differences between our modelling and that in Ref. 21. However, it is also possible that a higher resolution analysis of the cases presented in Ref. 21 might reveal the same pattern of behavior observed here. Such a test to see if Ref. 21 can be reconciled with our results merits investigation as this would clarify the possible topologies of the nucleation pathway in TSN. As mentioned earlier, our observation of spinodals bracketing the FPT is consistent with the analysis of Harrowell on the stability of sub-critical crystal nuclei,⁶⁰ and so it would be useful to assess the generality of this result by re-examining the features of the FES as presented in both Refs. 17 and 21.

A recent example consistent with the pattern of behavior shown here is the simulation study by Santra, Singh, and Bagchi,⁴¹ which focusses on the competition between BCC and FCC crystal nucleation in a hard-core repulsive Yukawa system. They showed that a post-critical BCC nucleus forms and grows spontaneously even under conditions where bulk FCC is the most stable phase. This case corresponds to the $n_c > n^*$ regime identified here. Reference 41 also evaluates 1D “cuts” through the FES, which in the terminology of this work correspond approximately to $f = 0$ (BCC-like) and $f = 1$ (FCC-like). Although the behavior of the 1D nucleation barriers so obtained is consistent with the 2D surfaces studied here, it would be useful to confirm this correspondence by computing the full 2D FES for the system studied in Ref. 41.

While several of the phenomena reported here have been documented in prior studies, these observations are fragmented across separate studies and are also limited in the

range of thermodynamic conditions examined. The general pattern of behavior presented here captures the key features of these earlier studies, clarifies the interrelationships of these findings, and also reveals important details of the FES not previously appreciated. We further show how the properties of the FES evolve over a wide range of thermodynamic conditions and correlate these changes to stable and metastable coexistence boundaries in the bulk phase diagram. Notably, no previous work has to our knowledge pointed out that the FPT is an intrinsic property of fluctuations and is distinct and independent from nucleation phenomena. Our work thus broadens, clarifies, and hopefully simplifies the conceptual framework for understanding the many phenomena associated with TSN.

VIII. DISCUSSION

In summary, we have attempted to clarify TSN by first disentangling the physics of the FPT from the nucleation process itself and showing that these are indeed distinct phenomena. We then examine how these two phenomena combine to produce TSN via a high-resolution study of the nucleation FES for a prototypical lattice model, conducted over a wide range of thermodynamic conditions.

To highlight the correspondence between the theoretical predictions of Sec. II and the realization of these predictions in our lattice model, we present in Fig. 14 a figure analogous to Fig. 1 but where the free energy is given by $\bar{G}(n)$ as computed

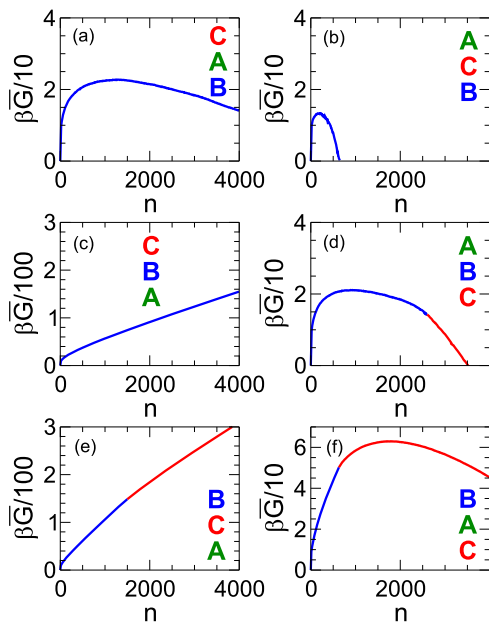


FIG. 14. $\bar{G}(n)$ at the six state points identified by open circles in the upper panel of Fig. 2 and representative of the six regions of the phase diagram labelled (a)–(f). The thermodynamic properties of the phases and their interfaces at each state point are given in Table I. To indicate the relative stability of the three bulk phases at each state point, the phases are listed vertically according to their value of μ , with μ increasing from bottom to top in each list. In each panel, $\bar{G}(n)$ is rendered in blue when $n < n_c$ and in red when $n > n_c$.

directly from our lattice model under conditions corresponding to each of the six regimes identified in Fig. 1. The six state points (a)–(f) examined in Fig. 14 are identified by the open circles in the phase diagram shown in the upper panel of Fig. 2. The thermodynamic properties of the phases at these state points, estimated as described in Secs. S3 and S4 of the supplementary material, are given in Table I. In Fig. 14, the curve for $\bar{G}(n)$ is blue when $n < n_c$ (where the nucleus is dominated by \mathcal{B}) and red when $n > n_c$ (where the nucleus is dominated by \mathcal{C}). In Fig. 1, the observed free energy will be either G_{AB} or G_{AC} , whichever is lower at a given n . In Fig. 14, the directly observed curve in each panel qualitatively matches the prediction from the corresponding panel in Fig. 1. The last column of Table I confirms that the condition in Eq. (3) is satisfied in all cases and, as predicted in Sec. II, we find that the nucleus starts out as a \mathcal{B} cluster at all six state points. Furthermore, in regions (d)–(f) of the phase diagram, an FPT occurs as the nucleus grows, regardless of whether the \mathcal{A} phase is stable [as in (e)] or metastable [as in (d) and (f)]. In region (d), the FPT occurs beyond the critical size, while in (f) it occurs before it.

Both our theoretical and simulation results thus demonstrate that under thermodynamic conditions commonly encountered in nucleation (e.g., near a triple point), the initial fluctuation of the system away from its equilibrium state takes the form of a local structure with the lowest surface tension with the surrounding phase. In other words, polymorph selection at the local level is under these conditions controlled by surface tension. When the lowest-surface-tension structure does not correspond to the most stable phase and Eq. (3) is satisfied, then the initial stage of nucleus growth will not resemble the stable phase and the result is TSN. The conversion of the fluctuation to the stable phase is a first-order FPT, which occurs by traversing a ridge in the FES. The transition state by which the system exits the metastable phase occurs at a saddle point in the FES and may occur before ($n_c < n^*$) or after ($n_c > n^*$) the FPT.

The Ostwald step rule (OSR) states that the bulk phase that forms first from a metastable phase is not the most stable phase but the phase with the chemical potential that is below but closest to the metastable phase.^{7,9,26,41} Our findings are consistent with the OSR but also provide a modified and more general way of understanding it. In our lattice model, when metastable \mathcal{A} transforms to stable \mathcal{C} , the \mathcal{B} phase always

TABLE I. Chemical potential μ of each phase and surface tension σ of the \mathcal{AB} and \mathcal{AC} interfaces, at each state point identified by the open circles in the upper panel of Fig. 2. These state points are representative of the six regimes of behavior labelled (a)–(f) in Figs. 1, 2, and 14. The quantity $\delta = \phi(\sigma_{AC} - \sigma_{AB}) - \Delta\mu_{CB}$ is positive if the condition in Eq. (3) is satisfied and negative if not.

Label	H	H_s	$\mu_{\mathcal{A}}/J$	$\mu_{\mathcal{B}}/J$	$\mu_{\mathcal{C}}/J$	$\sigma_{\mathcal{AB}}/J$	$\sigma_{\mathcal{AC}}/J$	δ/J
(a)	4.01	−0.01	−0.0105	−0.0207	0.0087	0.195	0.544	1.265
(b)	4.01	0.01	0.0087	−0.0207	−0.0105	0.195	0.544	1.246
(c)	3.98	−0.02	−0.0189	0.0070	0.0195	0.195	0.662	1.667
(d)	3.98	0.02	0.0195	0.0070	−0.0189	0.195	0.662	1.628
(e)	3.92	−0.02	−0.0164	0.0625	0.0220	0.195	0.850	2.281
(f)	3.92	0.02	0.0220	0.0625	−0.0164	0.195	0.850	2.242

appears first at the local level, regardless of whether \mathcal{B} has a higher or lower chemical potential. It is the low \mathcal{AB} surface tension that ensures that \mathcal{B} forms first within \mathcal{A} ; their relative chemical potentials are initially irrelevant. When $n_c < n^*$, the initial sub-critical nucleus resembles the \mathcal{B} phase, but because the FPT occurs prior to the transition state, there is no indication in the post-critical nucleus that the \mathcal{B} phase was initially dominant. However, when $n_c > n^*$, the post-critical nucleus resembles the \mathcal{B} phase, creating the conditions in which the OSR may be realized. The OSR is formally obeyed in our model phase diagram in the region bounded by \mathcal{L}_{AB} , \mathcal{L}_{BC} , and the LOM of the \mathcal{B} phase (region “O₁” in Fig. 2) because this is the region in which \mathcal{B} is both observable as a bulk metastable phase and also has a lower chemical potential than \mathcal{A} . At points in the phase diagram between \mathcal{L}_{AB} and \mathcal{L}_{BC} but beyond the LOM of the \mathcal{B} phase (region “O₂” in Fig. 2), the bulk \mathcal{B} phase is unstable. In this region, the post-critical nucleus will resemble \mathcal{B} but must convert to the stable \mathcal{C} phase at a finite size that is smaller than the system size. Thus the observation of behavior that obeys the OSR depends on an interplay of system-size effects (which control the location of the LOM) and the range of n_{\max} for the growing post-critical nucleus over which the low- f channel in the FES remains well-defined (which is controlled by the location of the spinodal on the low- f channel). In this study, we have restricted our evaluation of the FES to the range of n_{\max} in which the largest fluctuation does not approach the system size. It would be useful for future work to extend the FES to larger n_{\max} to further clarify the behavior related to the OSR.

As noted, the two steps in TSN are qualitatively different. One crosses a saddle point in the FES, and the other crosses a ridge. As such, both steps are activated processes. At the same time, the process that takes the system over the saddle point is similar to that in conventional (i.e., one-step) nucleation, while the ridge-crossing process of the FPT is more complex. The FPT occurs in a system (the fluctuation) the size of which is spontaneously increasing or decreasing, depending on the shape of the FES. Furthermore, there is a well-defined critical size for the nucleus of the stable phase to form inside the fluctuation, and until the fluctuation itself reaches this size, the stable phase will not be observed. This interplay of size effects is consistent with the existence of the spinodal limit of the high- f channel on the FES that prevents a \mathcal{C} -like fluctuation from being stable at small n_{\max} and suggests that this phenomenon is indeed general.⁶⁰ In addition, the existence of a spinodal limit at large n_{\max} along the low- f channel means that if the growing \mathcal{B} nucleus does not cross the ridge to the \mathcal{C} phase, then it will ultimately do so via a barrierless process at the spinodal. That is, the activated nature of the ridge-crossing FPT process is lost if the \mathcal{B} nucleus grows sufficiently large.

We also emphasize that this work explicitly considers only the thermodynamic aspects of TSN and that our conclusions apply to a system in which all degrees of freedom are sampled in equilibrium. We have not modelled kinetic effects, which are well known to play an important role in phase transitions generally. For example, in a bulk phase transition from a supercooled liquid to a crystal, sluggish kinetics may

completely prevent the formation of the thermodynamically-favored crystal phase on laboratory time scales, resulting in glass formation. Similarly, if the relaxation time for variations in f near a FPT greatly exceed the time scale for changes in the size of a fluctuation, the FPT may never be observed. In the case of our lattice model when $n_c > n^*$ [e.g., Fig. 8(c)], this effect would cause the system to be kinetically trapped in the low- f channel of the FES, resulting in the formation of the metastable \mathcal{B} phase, despite the greater thermodynamic stability of the \mathcal{C} phase. Previous simulation studies have demonstrated the existence of such kinetic effects during nucleation. For example, Ref. 68 presents the case of a binary mixture of charged colloids where the nucleation of a charge-disordered fcc bulk phase is observed under conditions where a charge-ordered bcc phase is both more stable and has a lower nucleation barrier. In this case, the relaxation of the local structure from disordered-fcc to ordered-bcc is too slow to occur on the time scale of nucleation, preventing the observation of the bcc phase. In a simulation study of diamond nucleation,⁶⁹ conditions were identified where the initial fluctuations of the melt were found to be similar to those of graphite rather than the more-stable diamond phase. This effect was attributed to the lower surface tension of the graphite-melt interface, compared to the diamond-melt interface, an observation in line with the predictions of this work. Furthermore, small graphite-like fluctuations were never observed to convert to the diamond structure, perhaps, because the kinetics for this process is too slow or perhaps because the most stable bulk structure (diamond) is thermodynamically unstable as a small fluctuation, as suggested by our lattice model results. These examples demonstrate both that dramatic kinetics effects are to be expected in TSN and also that a clearer understanding of the thermodynamic landscape underlying the nucleation process is critical for interpreting these kinetics effects.

We note further that all of our analysis concerning TSN assumes that the intermediate phase (\mathcal{B}) completely wets the stable phase (\mathcal{A}), a condition realized in our lattice model. An important direction for future work is to generalize these considerations to cases in which incomplete wetting occurs. In addition, the lattice model results presented here are all obtained at fixed T . While this constraint has simplified our analysis, now that the characteristics of the model FES have been described in detail, it will be interesting in subsequent studies to explore the T dependence of these features, especially for the FPT itself.

Our work also has a number of practical implications for simulation studies of nucleation. It is widely appreciated that care must be taken when choosing a local order parameter to define the nucleus, the size of which serves as the reaction coordinate in many studies which evaluate the nucleation barrier.^{57,58,70,71} Our results show that when this order parameter recognizes both the intermediate and the stable phase contributions to the nucleus, the “kink” in G_1 is a characteristic signature of TSN, which also locates n_c . Such a kink may be discerned in previous studies; see, e.g., Fig. 2 of Ref. 32. Conversely, caution must be exercised when conducting 1D umbrella sampling with respect to n_{\max} : If n_c is large, then

the barrier between the low- f and high- f channels will also be large, and so a series of simulations of progressively larger n_{\max} may become trapped in the low- f channel even when $n_{\max} > n_c$. When practical, 2D umbrella sampling to compute the full FES should be carried out, to ensure that the complete nucleation pathway is observed. It is also common to choose a local order parameter which only detects a nucleus of the stable phase. Our work demonstrates that when TSN occurs, the initial nuclei generated by this approach will not correspond to the most probable initial nuclei, resulting in a distortion in the shape of G_1 at small n . Where possible, a local order parameter should be chosen that identifies all structures that deviate from the metastable phase, not just those that resemble the stable phase. Recent work suggests that such an approach is feasible in molecular systems.⁷² Finally, we note the challenges that will be associated with estimating the nucleation rate from transition state theory when the transition state is not sharply defined in the FES, as in Fig. 8(b).⁵⁸ This difficulty may help explain the large deviations between estimated and observed nucleation rates noted for many systems exhibiting complex nucleation processes.^{7,23}

In addition, it is notable that in our lattice model we observe conditions where the most probable fluctuation of a given size does not correspond to a stable bulk phase under the same conditions, i.e., conditions beyond the LOM of the bulk phase. Sear noted a similar effect in a simulation study of heterogeneous nucleation.⁶⁶ It is therefore conceivable that, in other systems, a local fluctuation that never corresponds to a bulk phase might play an important role in the growth of the nucleus. Such fluctuations might include amorphous solid clusters or spatially limited structures such as icosahedra.³ This possibility, combined with the activated nature of the FPT, could account for long-lived metastable “prenucleation clusters” that grow to mesoscopic size before conversion to the stable phase, as has been reported, e.g., in crystallization of CaCO_3 .^{15,16,22,27}

We have shown that the dominant contribution of the surface tension to the free energy of small fluctuations underlies and explains the complexities of TSN observed near the triple point of our model system. Recent work on the competition between glass and crystal formation in supercooled liquids also points to the central role of low-surface-tension fluctuations,⁷⁵ which if different from the stable crystal can promote glass formation. The controlling influence of the surface tension in determining the most probable initial deviation from equilibrium may therefore be a principle with wide ranging implications for the behavior of metastable systems.

SUPPLEMENTARY MATERIAL

See [supplementary material](#) for a description of the details of our simulation methods and for additional plots of the free energy surface $G(n_{\max}, f)$.

ACKNOWLEDGMENTS

I.S.-V., R.K.B., and P.H.P. thank NSERC for support. P.H.P. also acknowledges the support from the Dr. W. F. James

Research Chair Program. Computational resources were provided by ACEnet and Compute Canada. We thank K. DeBell, D. Eaton, K. M. Poduska, F. Sciortino, and R. Timmons for helpful discussions.

REFERENCES

- H. E. Stanley, *Introduction to Phase Transitions and Critical Phenomena* (Oxford University Press, Oxford, 1971).
- L. Berthier and G. Biroli, *Rev. Mod. Phys.* **83**, 587 (2011).
- C. P. Royall and S. R. Williams, *Phys. Rep.* **560**, 1 (2015).
- F. Turci, C. P. Royall, and T. Speck, *Phys. Rev. X* **7**, 031028 (2017).
- M. A. Anisimov, M. Duška, F. Caupin, L. E. Amrhein, A. Rosenbaum, and R. J. Sadus, *Phys. Rev. X* **8**, 011004 (2018).
- P. G. Debenedetti, *Metastable Liquids. Concepts and Principles* (Princeton University Press, Princeton, New Jersey, 1996).
- K. F. Kelton and A. L. Greer, *Nucleation in Condensed Matter. Applications in Materials and Biology* (Elsevier, Oxford, 2010).
- P. R. ten Wolde and D. Frenkel, *Science* **277**, 1975 (1997).
- Z. Tavassoli and R. P. Sear, *J. Chem. Phys.* **116**, 5066 (2002).
- P. G. Vekilov, *Cryst. Growth Des.* **4**, 671 (2004).
- W. Pan, A. B. Kolomeisky, and P. G. Vekilov, *J. Chem. Phys.* **122**, 174905 (2005).
- J. F. Lutsko and G. Nicolis, *Phys. Rev. Lett.* **96**, 046102 (2006).
- J. A. van Meel, A. J. Page, R. P. Sear, and D. Frenkel, *J. Chem. Phys.* **129**, 204505 (2008).
- B. Chen, H. Kim, S. J. Keasler, and R. B. Nellas, *J. Phys. Chem. B* **112**, 4067 (2008).
- D. Gebauer, A. Völkel, and H. Kölfen, *Science* **322**, 1819 (2008).
- E. M. Pouget, P. H. H. Bomans, J. A. C. M. Goos, P. M. Frederik, G. de With, and N. A. J. M. Sommerdijk, *Science* **323**, 1455 (2009).
- N. Duff and B. Peters, *J. Chem. Phys.* **131**, 184101 (2009).
- P. G. Vekilov, *Nanoscale* **2**, 2346 (2010).
- S. Whitelam, *J. Chem. Phys.* **132**, 194901 (2010).
- L. O. Hedges and S. Whitelam, *J. Chem. Phys.* **135**, 164902 (2011).
- M. Iwamatsu, *J. Chem. Phys.* **134**, 164508 (2011).
- R. Demichelis, P. Raiteri, D. Quigley, D. Gebauer, and J. D. Gale, *Nat. Commun.* **2**, 590 (2011).
- R. P. Sear, *Int. Mater. Rev.* **57**, 328 (2012).
- M. Iwamatsu, *Phys. Rev. E* **86**, 041604 (2012).
- M. Iwamatsu, *J. Chem. Phys.* **136**, 044701 (2012).
- M. Santra, R. S. Singh, and B. Bagchi, *J. Phys. Chem. B* **117**, 13154 (2013).
- A. F. Wallace, L. O. Hedges, A. Fernandez-Martinez, P. Raiteri, J. D. Gale, G. A. Waychunas, S. Whitelam, J. F. Banfield, and J. J. De Yoreo, *Science* **341**, 885 (2013).
- Y. Peng, F. Wang, Z. Wang, A. M. Alsayed, Z. Zhang, A. G. Yodh, and Y. Han, *Nat. Mater.* **14**, 101 (2014).
- M. Salvalaglio, C. Perego, F. Giberti, M. Mazzotti, and M. Parrinello, *Proc. Natl. Acad. Sci. U. S. A.* **112**, E6 (2015).
- K. Kratzer and A. Arnold, *Soft Matter* **11**, 2174 (2015).
- S. M. A. Malek, G. P. Morrow, and I. Saika-Voivod, *J. Chem. Phys.* **142**, 124506 (2015).
- W. Qi, Y. Peng, Y. Han, R. K. Bowles, and M. Dijkstra, *Phys. Rev. Lett.* **115**, 185701 (2015).
- G. C. Sosso, J. Chen, S. J. Cox, M. Fitzner, P. Pedevilla, A. Zen, and A. Michaelides, *Chem. Rev.* **116**, 7078 (2016).
- S. Ishizuka, Y. Kimura, T. Yamazaki, T. Hama, N. Watanabe, and A. Kouchi, *Chem. Mater.* **28**, 8732 (2016).
- C. Guo, J. Wang, J. Li, Z. Wang, and S. Tang, *J. Phys. Chem. Lett.* **7**, 5008 (2016).
- Y. Bi, A. Porras, and T. Li, *J. Chem. Phys.* **145**, 211909 (2016).
- M. Iwamatsu, *Phys. Rev. E* **95**, 042803 (2017).
- C.-T. Lee and E. M. Terentjev, *J. Chem. Phys.* **147**, 105103 (2017).

- ³⁹F. Zhang, *J. Phys.: Condens. Matter* **29**, 443002 (2017).
- ⁴⁰T. Yamazaki, Y. Kimura, P. G. Vekilov, E. Furukawa, M. Shirai, H. Matsumoto, A. E. S. Van Driessche, and K. Tsukamoto, *Proc. Natl. Acad. Sci. U. S. A.* **114**, 2154 (2017).
- ⁴¹M. Santra, R. S. Singh, and B. Bagchi, *Phys. Rev. E* **98**, 032606 (2018).
- ⁴²A. E. S. Van Driessche, N. Van Gerven, P. H. H. Bomans, R. R. M. Joosten, H. Friedrich, D. Gil-Carton, N. A. J. M. Sommerdijk, and M. Sleutel, *Nature* **556**, 89 (2018).
- ⁴³K. Binder and D. Landau, *A Guide to Monte Carlo Simulations in Statistical Physics*, 3rd ed. (Cambridge University Press, New York, 2009).
- ⁴⁴D. P. Landau, *Phys. Rev. Lett.* **28**, 449 (1972).
- ⁴⁵D. P. Landau and R. H. Swendsen, *Phys. Rev. Lett.* **46**, 1437 (1981).
- ⁴⁶P. A. Rikvold, W. Kinzel, J. D. Gunton, and K. Kaski, *Phys. Rev. B* **28**, 2686 (1983).
- ⁴⁷H. J. Herrmann, *Phys. Lett. A* **100**, 256 (1984).
- ⁴⁸D. P. Landau and R. H. Swendsen, *Phys. Rev. B* **33**, 7700 (1986).
- ⁴⁹C. Borgs and R. Kotecký, *J. Stat. Phys.* **61**, 79 (1990).
- ⁵⁰K. Binder, *Eur. Phys. J. B* **64**, 307 (2008).
- ⁵¹M. E. Tuckerman, *Statistical Mechanics: Theory and Molecular Simulation* (Oxford University Press, Oxford, 2010).
- ⁵²K. Binder, B. Block, S. K. Das, P. Virnau, and D. Winter, *J. Stat. Phys.* **144**, 690 (2011).
- ⁵³K. Binder, B. J. Block, P. Virnau, and A. Tröster, *Am. J. Phys.* **80**, 1099 (2012).
- ⁵⁴S. Ryu and W. Cai, *Phys. Rev. E* **81**, 030601 (2010).
- ⁵⁵S. Kumar, D. Bouzida, R. H. Swendsen, P. A. Kollman, and J. M. Rosenberg, *J. Comput. Chem.* **13**, 1011 (1992).
- ⁵⁶A. Grossfield, WHAM: The Weighted Histogram Analysis Method, Version 2.0.9, 2018, <http://membrane.urmc.rochester.edu/content/wham>.
- ⁵⁷P. R. ten Wolde, M. J. Ruiz-Montero, and D. Frenkel, *Faraday Discuss.* **104**, 93 (1996).
- ⁵⁸S. Auer and D. Frenkel, *J. Chem. Phys.* **120**, 3015 (2004).
- ⁵⁹S. E. M. Lundrigan and I. Saika-Voivod, *J. Chem. Phys.* **131**, 104503 (2009).
- ⁶⁰P. Harrowell, *J. Phys.: Condens. Matter* **22**, 364106 (2010).
- ⁶¹R. Sear, *J. Phys.: Condens. Matter* **17**, 3997 (2005).
- ⁶²A. J. Page and R. P. Sear, *Phys. Rev. Lett.* **97**, 065701 (2006).
- ⁶³R. P. Sear, *J. Phys.: Condens. Matter* **19**, 466106 (2007).
- ⁶⁴R. P. Sear, *J. Chem. Phys.* **129**, 164510 (2008).
- ⁶⁵R. P. Sear, *Europhys. Lett.* **83**, 66002 (2008).
- ⁶⁶R. P. Sear, *J. Chem. Phys.* **131**, 074702 (2009).
- ⁶⁷R. P. Sear, *J. Phys.: Condens. Matter* **24**, 052205 (2011).
- ⁶⁸E. Sanz, C. Valeriani, D. Frenkel, and M. Dijkstra, *Phys. Rev. Lett.* **99**, 055501 (2007).
- ⁶⁹L. Ghiringhelli, C. Valeriani, E. Meijer, and D. Frenkel, *Phys. Rev. Lett.* **99**, 055702 (2007).
- ⁷⁰L. C. Jacobson, M. Matsumoto, and V. Molinero, *J. Chem. Phys.* **135**, 074501 (2011).
- ⁷¹A. Reinhardt, J. P. K. Doye, E. G. Noya, and C. Vega, *J. Chem. Phys.* **137**, 194504 (2012).
- ⁷²Z. Krebs, A. B. Roitman, L. M. Nowack, C. Liepold, B. Lin, and S. A. Rice, *J. Chem. Phys.* **149**, 034503 (2018).
- ⁷³J. Russo, F. Romano, and H. Tanaka, *Phys. Rev. X* **8**, 021040 (2018).

SUPPLEMENTAL MATERIAL

Phase transitions in fluctuations and their role in two-step nucleation

D. James, S. Beairsto, C. Hartt, O. Zavalov, I. Saika-Voivod, R.K. Bowles and P.H. Poole

December 17, 2018

S1. PHASE DIAGRAM

To evaluate the phase diagram of our lattice model, we use umbrella sampling MC simulations to compute the system free energy as a function of two bulk order parameters, the magnetization m and the staggered magnetization m_s [43, 51]. These are defined as,

$$m = \frac{1}{N} \sum_{i=1}^N s_i \quad (\text{S1})$$

$$m_s = \frac{1}{N} \sum_{i=1}^N \sigma_i s_i. \quad (\text{S2})$$

Note that m and m_s are subject to the constraints,

$$\begin{aligned} m + m_s &\leq 1 \\ m - m_s &\leq 1. \end{aligned} \quad (\text{S3})$$

The order parameters m and m_s can be used to identify each of the phases in our system. At $T = 0$, four phases are observed, depending on the values of H and H_s : two ferromagnetically ordered phases with $(m, m_s) = (-1, 0)$ and $(m, m_s) = (1, 0)$, denoted respectively as $\bar{\mathcal{B}}$ and \mathcal{B} ; and two antiferromagnetically ordered phases with $(m, m_s) = (0, -1)$ and $(m, m_s) = (0, 1)$, denoted respectively as \mathcal{A} and \mathcal{C} . Since we only consider $H > 0$, the $\bar{\mathcal{B}}$ phase does not appear in our analysis.

To locate stability fields and phase boundaries for each phase, we evaluate,

$$\beta G(m_s, m) = -\log[P(m_s, m)] + C, \quad (\text{S4})$$

where $G(m_s, m)$ is the conditional free energy of the system at fixed (H_s, H, T) as a function of m_s and m . $P(m_s, m)$ is a function that is proportional to the probability of observing a

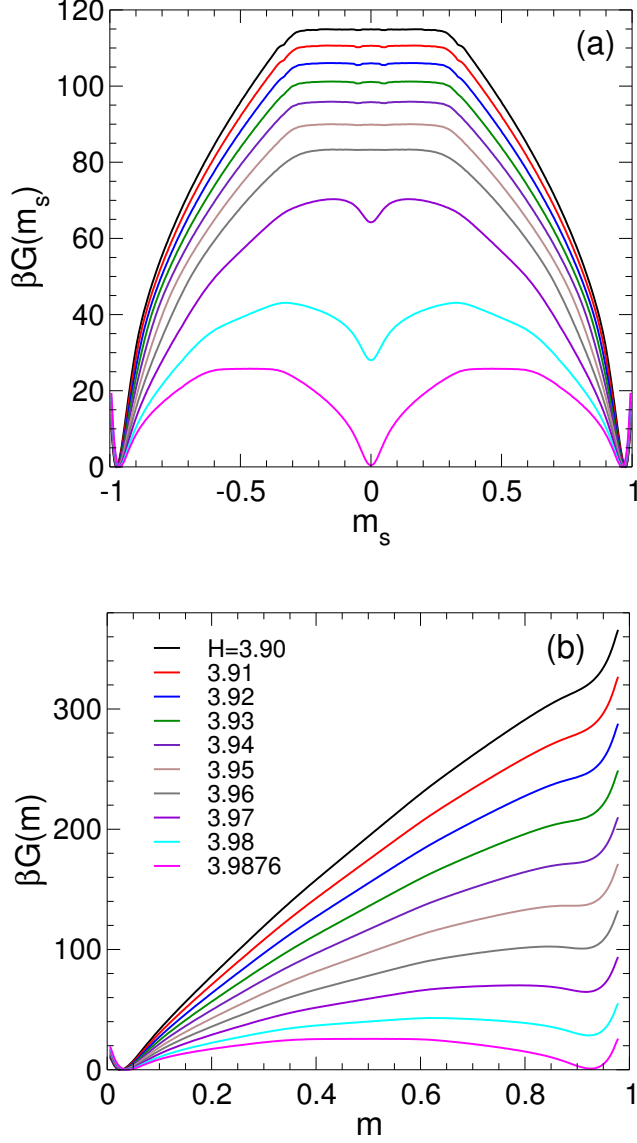


FIG. S1. (a) $G(m_s)$ and (b) $G(m)$ along the \mathcal{AC} coexistence curve (where $H_s = 0$) for a system with $L = 64$. The legend given in (b) applies to both panels.

given value of m_s and m under the same conditions of (H_s, H, T) . The value of the arbitrary constant C in Eq. S4, and in all subsequent equations in which it occurs, is always chosen so that the global minimum of the corresponding free energy is zero. We also define,

$$\begin{aligned} \beta G(m_s) &= -\log[P(m_s)] + C \\ P(m_s) &= \int_0^1 P(m_s, m) dm, \end{aligned} \quad (\text{S5})$$

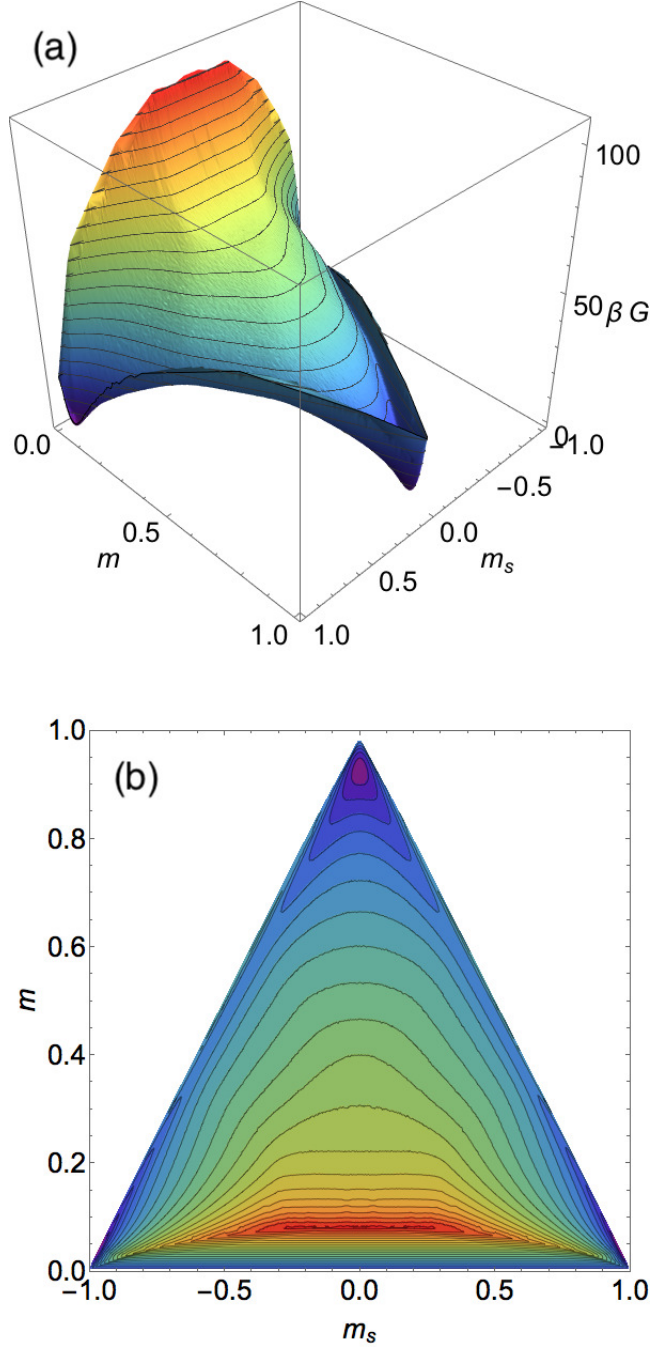


FIG. S2. $G(m_s, m)$ at the triple point for a system with $L = 64$. Contours are $5kT$ apart. Panel (a) is a surface plot of $G(m_s, m)$ and panel (b) is a contour plot of the same data.

and,

$$\begin{aligned}
 \beta G(m) &= -\log[P(m)] + C \\
 P(m) &= \int_{-1}^1 P(m_s, m) dm_s.
 \end{aligned}
 \tag{S6}$$

We estimate $P(m_s, m)$ from umbrella sampling simulations using a biasing potential,

$$U'_B = \kappa_s(m_s - m_s^*)^2 + \kappa_m(m - m^*)^2, \quad (\text{S7})$$

where m_s^* and m^* specify the target values of m_s and m to be sampled, and κ_s and κ_m control the range of sampling around the target values. All our umbrella sampling simulations using U'_B are carried out with a system size of $L = 64$ and at the state point $(H_s^0, H^0, kT/J) = (0, 3.9875, 1)$. As we will see below, this point is on the \mathcal{AC} coexistence line and is very close to the \mathcal{ABC} triple point. Since this point is on the $H_s = 0$ axis, we only need to compute $P(m_s, m)$ for $0 < m_s < 1$ because $P(m_s, m) = P(-m_s, m)$ under these conditions. Also, since $m_s + m \leq 1$, the range of $P(m_s, m)$ is further restricted to the triangle-shaped region bounded by $m_s = 0$, $m = 0$, and $m_s + m = 1$. We cover this region using 903 umbrella windows with $m_s^* = 100i/L^2$ where i is an integer in the range $[0, 41]$, and $m^* = 100j/L^2$ where j is an integer in the range $[0, 41 - i]$. We choose $\kappa_s = \kappa_m = 0.0005L^4J$. Trial configurations are accepted or rejected using the umbrella potential every 1 MCS. In all of our simulations, one MCS corresponds to L^2 attempts to flip the spin of a randomly chosen lattice site. The simulation for each umbrella window is initialized using a perfect \mathcal{C} configuration. Each run is equilibrated for 2×10^5 MCS, after which m_s and m are recorded every 400 MCS for the next 4×10^6 MCS.

The time series of m_s and m for all umbrella simulations are analyzed and combined using WHAM [55, 56] to generate estimates of $P(m_s, m)$ and $G(m_s, m)$ at $(H_s^0, H^0, kT/J) = (0, 3.9875, 1)$. For the WHAM analysis, we exclude every run with an umbrella sampling acceptance rate of less than 0.04. This reduces the number of windows analyzed to 819. The windows excluded are: $j = 0$ and $0 \leq i \leq 33$; $j = 1$ and $0 \leq i \leq 28$; and $j = 2$ and $0 \leq i \leq 20$. These windows correspond to regions in which $G(m_s, m)$ is very large and steep, and which make a negligible contribution to the average properties of equilibrium states near the triple point. We estimate that the error in our computed values for $G(m_s, m)$ is at most $1kT$.

$P(m_s, m)$ provides the complete density of states as a function of m_s and m , and can be used to find $P(m_s, m)$ or $G(m_s, m)$ at nearby values of (H_s, H) by reweighting according to,

$$G(m_s, m; H_s, H)/J = G(m_s, m; H_s^0, H^0)/J - N(H_s - H_s^0)m_s - N(H - H^0)m. \quad (\text{S8})$$

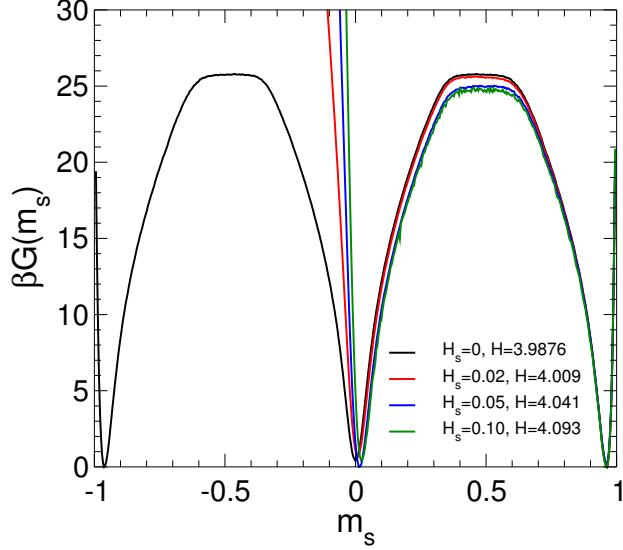


FIG. S3. $G(m_s)$ along the \mathcal{BC} coexistence curve for an $L = 64$ system.

Having reweighted $G(m_s, m)$ to new values of (H_s, H) , we can also obtain $G(m_s)$ and $G(m)$ at the same (H_s, H) .

Due to the symmetry of the system Hamiltonian, the \mathcal{AC} coexistence line lies on the $H_s = 0$ axis and so the value of H_s at the \mathcal{ABC} triple point is $H_s^T = 0$. At the triple point, $G(m_s, m)$ will exhibit three basins of approximately equal depth, one for each of the phases \mathcal{A} , \mathcal{B} and \mathcal{C} . We further note that when $H > 0$ and the $\bar{\mathcal{B}}$ phase can be ignored, m_s by itself serves as an order parameter to distinguish each phase, since $m_s \simeq -1$ in \mathcal{A} , $m_s \simeq 0$ in \mathcal{B} , and $m_s \simeq 1$ in \mathcal{C} . At the triple point, $G(m_s)$ will therefore also display three minima of approximately equal depth. In Fig. S1(a) we show $G(m_s)$ at $H_s = 0$ for several H approaching the triple point, where we observe the emergence of these three minima. To precisely locate H^T , the value of H at the triple point, we evaluate $P(m_s)$ at several values of H and seek conditions where the areas under the three peaks in $P(m_s)$ corresponding to each phase are equal [49, 50]. We find $H^T = 3.9876 \pm 0.0005$. Fig. S1 shows $G(m_s)$ and $G(m)$ at the triple point, and Fig. S2 shows $G(m_s, m)$ at the triple point.

We locate points on the \mathcal{BC} coexistence curve by examining the behavior of $G(m_s)$ and $P(m_s)$ at several fixed values of $H_s > 0$. For a given value of H_s , we seek the value of H at which the areas under the peaks in $P(m_s)$ for the \mathcal{B} and \mathcal{C} phases are equal. Fig. S3 shows $G(m_s)$ at several points on the \mathcal{BC} coexistence curve determined in this way, confirming that under these conditions the minima for the \mathcal{B} and \mathcal{C} phases are of approximately equal depth. The result for the \mathcal{BC} coexistence curve is shown in Fig. 2, for which the statistical

error in H is 0.0005. The \mathcal{AB} coexistence curve in Fig. 2 is simply the reflection of the \mathcal{BC} coexistence curve about the $H_s = 0$ axis.

S2. LIMIT OF METASTABILITY OF THE \mathcal{B} PHASE

As shown in Fig. S1(b), at $H_s = 0$ a local minimum corresponding to the \mathcal{B} phase occurs in $G(m)$ in the vicinity of $m \simeq 0.95$. This minimum persists even for values of H outside of the stability field of \mathcal{B} , i.e. for values of H below the triple point. Under these conditions, this minimum of $G(m)$ corresponds to the metastable bulk \mathcal{B} phase. As H decreases further this minimum disappears, thus defining the limit of metastability (LOM) of the bulk \mathcal{B} phase. We locate the LOM of the \mathcal{B} phase in the phase diagram by seeking the value of H at which the local minimum for \mathcal{B} in $G(m)$ disappears with decreasing H at several fixed values of H_s . The result for a system of size $L = 64$ is shown in Fig. 2. Note the LOM is system-size dependent. As $L \rightarrow \infty$, the LOM approaches the \mathcal{BC} and \mathcal{AB} coexistence curves [53].

S3. CHEMICAL POTENTIAL OF BULK PHASES AND METASTABLE PHASE BOUNDARIES

We estimate the chemical potential of each bulk phase at a given value of (H_s, H) , relative to its value at the triple point, using,

$$\bar{\mu}_{\mathcal{A}}(H_s, H) = -\frac{kT}{N} \log \left(\int_{-1}^{-0.9} dm_s \int_0^1 dm \exp[-\beta G(m_s, m; H_s, H)] \right) - \bar{\mu}_{\mathcal{A}}^0 \quad (\text{S9})$$

$$\bar{\mu}_{\mathcal{B}}(H_s, H) = -\frac{kT}{N} \log \left(\int_{-1}^1 dm_s \int_{0.9}^1 dm \exp[-\beta G(m_s, m; H_s, H)] \right) - \bar{\mu}_{\mathcal{B}}^0 \quad (\text{S10})$$

$$\bar{\mu}_{\mathcal{C}}(H_s, H) = -\frac{kT}{N} \log \left(\int_{0.9}^1 dm_s \int_0^1 dm \exp[-\beta G(m_s, m; H_s, H)] \right) - \bar{\mu}_{\mathcal{C}}^0, \quad (\text{S11})$$

where $\bar{\mu}_{\mathcal{A}}^0$ is chosen such that $\bar{\mu}_{\mathcal{A}}(H_s^T, H^T) = 0$, and similarly for $\bar{\mu}_{\mathcal{B}}^0$ and $\bar{\mu}_{\mathcal{C}}^0$. The integrals in the above relations sum over a region of the (m_s, m) plane which encompasses the minimum of the basin for the corresponding phase, and in which the system is a single homogeneous

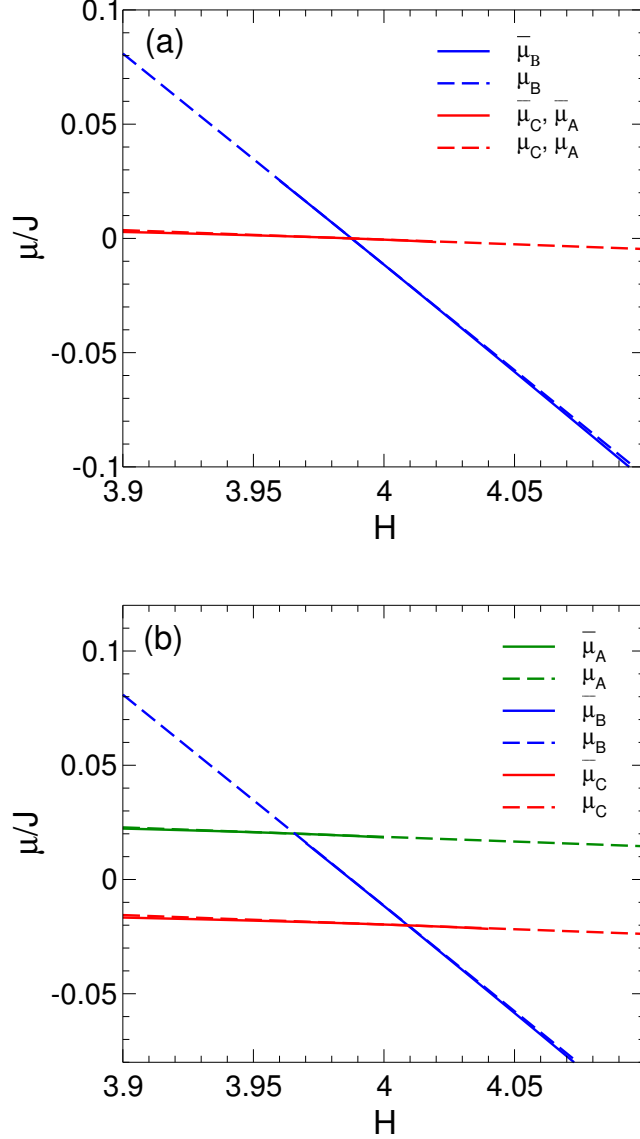


FIG. S4. Chemical potentials of bulk phases as a function of H at fixed H_s . Solid lines end at the limit of metastability for the bulk phase in a system with $L = 64$. In (a) $H_s = 0$, and in (b) $H_s = 0.02$. Note that when $H_s = 0$, $\mu_A = \mu_C$.

phase. In Fig. S4 we plot $\bar{\mu}_A$, $\bar{\mu}_B$ and $\bar{\mu}_C$ as a function of H at $H_s = 0$ and $H_s = 0.02$. These lines terminate at the value of H for the LOM of each phase for our $L = 64$ system, i.e. where the local minimum in $G(m_s, m; H_s, H)$ ceases to exist.

Although the chemical potential is always well defined within the stability field of each phase, for a metastable bulk phase it is only defined when a local minimum is observed in $G(m_s, m; H_s, H)$. However, for the purpose of analyzing the nucleation behavior predicted by Eq. 1, it would be useful to have an approximate way to assign a value to the chemical potential for a phase that is beyond its LOM. We find that it is possible to do so in our

lattice model because the dependence of $\bar{\mu}$ on H_s and H is very close to linear for all three phases; see Fig. S4. As a simple approximation, we therefore model the chemical potential for each phase, relative to the triple point, using the expressions:

$$\mu_{\mathcal{A}}(H_s, H)/J = -(H_s - H_s^T)m_s^{\mathcal{A}} - (H - H^T)m^{\mathcal{A}} \quad (\text{S12})$$

$$\mu_{\mathcal{B}}(H_s, H)/J = -(H_s - H_s^T)m_s^{\mathcal{B}} - (H - H^T)m^{\mathcal{B}} \quad (\text{S13})$$

$$\mu_{\mathcal{C}}(H_s, H)/J = -(H_s - H_s^T)m_s^{\mathcal{C}} - (H - H^T)m^{\mathcal{C}}. \quad (\text{S14})$$

In these relations, we use the value of m_s and m for each phase at the triple point to fix the rate of change of μ with H_s or H , since $m_s = -(\partial\mu/\partial H_s)_{H,T}$ and $m = -(\partial\mu/\partial H)_{H_s,T}$. At the triple point, the average value of m_s and m for the \mathcal{A} phase is $m_s^{\mathcal{A}} = -0.959$ and $m^{\mathcal{A}} = 0.0413$; for the \mathcal{B} phase is $m_s^{\mathcal{B}} = 0$ and $m^{\mathcal{B}} = 0.924$; and for the \mathcal{C} phase is $m_s^{\mathcal{C}} = -m_s^{\mathcal{A}}$ and $m^{\mathcal{C}} = m^{\mathcal{A}}$. We compare $\bar{\mu}$ and μ for each phase in Fig. S4, and find that these two approaches give nearly indistinguishable results. The metastable extensions of the coexistence boundaries shown in Fig. 2 are estimated by finding the intersection of the surfaces defined in Eqs. S12-S14.

Note that since $m^{\mathcal{C}} = m^{\mathcal{A}}$, then $\Delta\mu_{\mathcal{AC}} = \mu_{\mathcal{C}} - \mu_{\mathcal{A}}$ does not depend on H and is constant at fixed H_s . In contrast, $\Delta\mu_{\mathcal{AB}} = \mu_{\mathcal{B}} - \mu_{\mathcal{A}}$ decreases linearly with H at fixed H_s . These observations are relevant for understanding the behavior of the CNT estimates for $n_{\mathcal{AB}}^*$ and $n_{\mathcal{AC}}^*$ plotted in Fig. 11.

S4. SURFACE TENSION

The surface tension (or interfacial free energy) σ between two coexisting phases can be estimated from the height of the free energy barrier that separates the two successive minima corresponding to the coexisting phases in a plot of $G(m_s)$ or $G(m)$ [50, 52, 53]. This approach provides a direct estimate of the surface tension because the free energy is evaluated as a function of an order parameter which is a continuous reaction coordinate connecting a free energy minimum, where the system is a single homogeneous phase, to a free energy maximum, where the systems consists of two coexisting phases separated by an interface. The thermodynamic work of formation of the interface is thus computed directly. As shown in Figs. S1 and S3, the top of this free energy barrier is flat for a system in

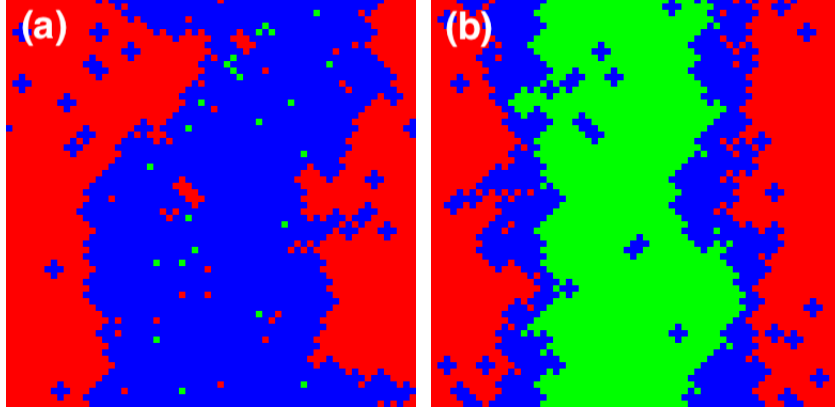


FIG. S5. (a) Snapshot of \mathcal{BC} coexistence at $H_s = 0$ and $H = 3.987$ in a system with $m_s \simeq 0.5$. (b) Snapshot of \mathcal{AC} coexistence at $H_s = 0$ and $H = 3.96$ in a system with $m_s \simeq 0$. $L = 64$ for both (a) and (b).

which two phases coexist, indicating the range of m_s or m values where two flat interfaces separate the two phases in our periodic system. Example snapshots of coexisting phases in our $L = 64$ simulations are shown in Fig. S5.

We define the interfacial free energy σ such that the height of the barrier in $\beta G(m_s)$ or $\beta G(m)$ is $2L\beta\sigma$; the factor of $2L$ accounts for the two interfaces that occur in a system with periodic boundaries. Fig. S3 shows that for the coexistence of \mathcal{B} and \mathcal{C} in a $L = 64$ system at the triple point conditions, $2L\beta\sigma_{\mathcal{BC}} = 25 \pm 1$, and exhibits little observable variation along the \mathcal{BC} coexistence curve in the range of H and H_s studied here.

In Fig. S6 we show $G(m)$ for various H at $H_s = 0$. For any H , $\sigma_{\mathcal{BC}}$ may be estimated from the difference between the $G(m)$ curve and a common-tangent line bounding the $G(m)$ curve from below, at a value of m corresponding to a coexisting system of \mathcal{B} and \mathcal{C} , e.g. $m = 0.5$. Further, at fixed H_s , if $G(m)$ is computed at one value of $H = H_1$, it can be found (up to an irrelevant constant C) at a new value $H = H_2$ using,

$$G(m; H_2)/J = G(m; H_1)/J - N(H_2 - H_1)m + C. \quad (\text{S15})$$

As a consequence of the form of Eq. S15, $\sigma_{\mathcal{BC}}$ is independent of H at fixed H_s . Also, since we have observed that $\sigma_{\mathcal{BC}}$ varies little on the \mathcal{BC} coexistence curve (Fig. S3), along which H_s is changing, we conclude that $\sigma_{\mathcal{BC}}$ is approximately constant for all H and H_s studied here.

Note that we obtain the same value of $\sigma_{\mathcal{BC}}$ (within error) when we analyze the height

of the barrier observed in either $G(m_s)$ in Fig. S3, or $G(m)$ in Fig. S6. This confirms that our estimate of the surface tension does not depend on the choice of m or m_s as the order parameter to distinguish between the \mathcal{B} phase and either of the \mathcal{A} or \mathcal{C} phases.

Furthermore, the symmetry of the system Hamiltonian ensures that $\sigma_{\mathcal{AB}} = \sigma_{\mathcal{BC}}$. That is, the \mathcal{A} and \mathcal{C} phases are structurally identical in that both are antiferromagnetic “checkerboard” phases. The only difference is that in the \mathcal{C} phase the spins are aligned with a positive staggered field, while in the \mathcal{A} phase they are anti-aligned. Thus the average structure of the interface of either the \mathcal{A} or \mathcal{C} phase with the all-up \mathcal{B} phase is the same; in either case, the interface is the boundary between a checkerboard phase and an all-up phase. The equality $\sigma_{\mathcal{AB}} = \sigma_{\mathcal{BC}}$ is numerically confirmed at the triple point in Fig. S1(a), where we see that the heights of the two free energy maxima in $G(m_s)$, which directly measure $\sigma_{\mathcal{AB}}$ and $\sigma_{\mathcal{BC}}$, are equal. Since we have also shown that $\sigma_{\mathcal{BC}}$ is independent of H and H_s , we can conclude that $\sigma_{\mathcal{AB}} = \sigma_{\mathcal{BC}}$ throughout our phase diagram. We thus use the value $2L\beta\sigma_{\mathcal{AB}} = 2L\beta\sigma_{\mathcal{BC}} = 25$, or $\sigma_{\mathcal{AB}}/J = \sigma_{\mathcal{BC}}/J = 0.195$ (per unit lattice site of interface) in all of our analysis.

We next estimate $\sigma_{\mathcal{AC}}$ as a function of H along the $H_s = 0$ axis for $H < H_T$. In Fig. S1(a) we plot $G(m_s)$ on the \mathcal{AC} coexistence curve at $H = 3.94$, a point at which the \mathcal{B} phase is unstable for a system of size $L = 64$. From the height of the free energy barrier separating the minima corresponding to the pure \mathcal{A} and \mathcal{C} phases, we find $2L\beta\sigma_{\mathcal{AC}} = 96 \pm 1$. We also directly estimate $\sigma_{\mathcal{AC}}$ for other values of H from the $G(m_s)$ curves in Fig. S1 that are flat near $m_s = 0$, and plot the results in Fig. S7.

To estimate $\sigma_{\mathcal{AC}}$ as a function of H along the entire \mathcal{AC} coexistence curve we use thermodynamic integration. That is, we choose as a reference value $H_0 = 3.94$ where we already know $\sigma_{\mathcal{AC}}$ from the direct calculation described above. We then use thermodynamic integration to estimate the change in the interfacial free energy as we move the system to a different value of H . On the \mathcal{AC} coexistence curve, the free energy of the pure \mathcal{A} and \mathcal{C} phases is the same. Under these conditions, the \mathcal{AC} surface tension is the difference between the free energy of a system containing an \mathcal{AC} interface and the free energy of a pure phase, either \mathcal{A} or \mathcal{C} , since the conversion of part of the system from \mathcal{A} to \mathcal{C} to create the coexisting system makes no bulk contribution to the free energy change. The change in the \mathcal{AC} surface tension on moving from H_0 to H is thus given by the difference between the change in the free energy of a system containing an \mathcal{AC} interface, and the change in the free energy of the

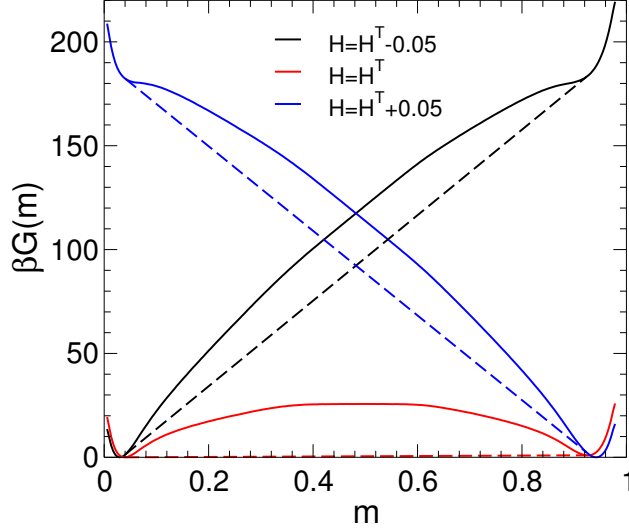


FIG. S6. $G(m)$ at $H_s = 0$ at various H for system size $L = 64$. Dashed lines are common tangent constructions for each $G(m)$ curve.

pure phase:

$$2L\sigma_{\mathcal{AC}}(H) - 2L\sigma_{\mathcal{AC}}(H_0) = \Delta G_{\text{coex}}(H) - \Delta G_{\mathcal{A}}(H). \quad (\text{S16})$$

The change in the free energy of a system containing an \mathcal{AC} interface on moving from H_0 to H is given by,

$$\Delta G_{\text{coex}}(H)/J = -N \int_{H_0}^H m_{\text{coex}}(H') dH'. \quad (\text{S17})$$

Here $m_{\text{coex}}(H)$ is the average magnetization of a system containing an \mathcal{AC} interface as a function of H . To estimate $m_{\text{coex}}(H)$, we evaluate m as a function of H for a coexisting system of \mathcal{A} and \mathcal{C} phases along the $H_s = 0$ coexistence curve. We constrain this coexisting system to remain within the range of m_s consistent with the occurrence of a pair of system-spanning \mathcal{AC} interfaces by applying a simple square-well biasing potential that prevents the system from sampling microstates with $|m_s| > 0.1$. In Eq. S16 we chose \mathcal{A} to represent the pure phase. Its free energy change on moving from H_0 to H is given by,

$$\Delta G_{\mathcal{A}}(H)/J = -N \int_{H_0}^H m_{\mathcal{A}}(H') dH', \quad (\text{S18})$$

where $m_{\mathcal{A}}(H)$ is the average magnetization of the pure \mathcal{A} phase as a function of H . To estimate $m_{\mathcal{A}}(H)$, we evaluate m as a function of H for the homogeneous \mathcal{A} phase along the $H_s = 0$ coexistence curve.

The result for $\sigma_{\mathcal{AC}}$ is shown in Fig. S7. We show snapshots of the coexisting \mathcal{A} and \mathcal{C}

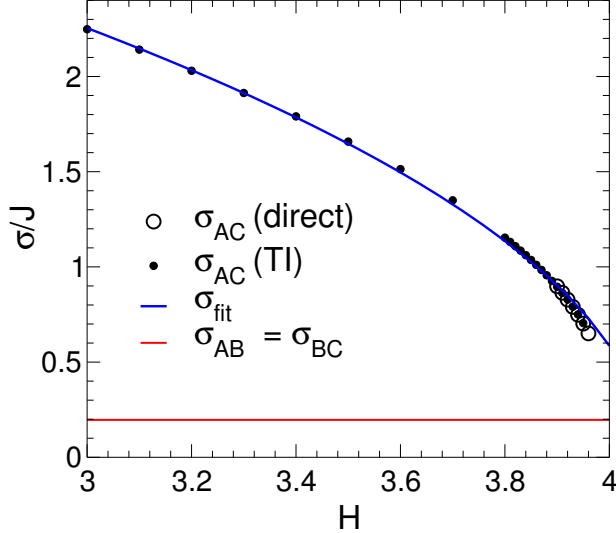


FIG. S7. Interfacial tensions versus H at $H_s = 0$ for $L = 64$. Open circles are values of $\sigma_{\mathcal{AC}}$ found directly from the plots of $G(m_s)$ presented in Fig. S1(a). Filled circles are values of $\sigma_{\mathcal{AC}}$ found by thermodynamic integration (TI) using Eq. S16. The blue curve is $\sigma_{\text{fit}}/J = (19.299 - 4.739H)^{1/2}$, fitted to data obtained via TI for $H = 2$ to $H = 4$. The red curve gives the value of $\sigma_{\mathcal{AB}} = \sigma_{\mathcal{BC}}$.

phases at different values of H in Fig. S8. We note the complexity of the \mathcal{AC} interface. Depending on H the interface may contain a significant wetting layer of \mathcal{B} between the \mathcal{A} and \mathcal{C} regions. Approaching the triple point $\sigma_{\mathcal{AC}}$ decreases but remains more than twice the value of $\sigma_{\mathcal{AB}}$ at the triple point. Given the emergence of the wetting layer of \mathcal{B} as $H \rightarrow H^T$, the behavior of $\sigma_{\mathcal{AC}}$ makes sense: In this regime the \mathcal{AC} interface can be approximated as the superposition two interfaces, one \mathcal{AB} and the other \mathcal{BC} . Since $\sigma_{\mathcal{AB}} = \sigma_{\mathcal{BC}}$, it therefore seems likely that the condition $\sigma_{\mathcal{AC}} \geq 2\sigma_{\mathcal{AB}}$ holds under all conditions studied here.

In order to compare the behavior of our lattice model to the predictions of CNT, it is useful to have an analytic model of the dependence of $\sigma_{\mathcal{AC}}$ on H_s and H throughout the phase diagram. By an argument analogous to that used above to establish that $\sigma_{\mathcal{BC}}$ is independent of H at constant H_s (see Eq. S15), it can be shown that $\sigma_{\mathcal{AC}}$ is independent of H_s at fixed H . To model the dependence of $\sigma_{\mathcal{AC}}$ on H , we notice empirically that $\sigma_{\mathcal{AC}}^2$ is approximately linear in H between $H = 2$ and 4. We fit a straight line to our data for $\sigma_{\mathcal{AC}}^2$ in this range and obtain $\sigma_{\text{fit}}/J = (19.299 - 4.739H)^{1/2}$, shown in Fig. S7. We use σ_{fit} to compute the CNT estimate of $n_{\mathcal{AC}}^*$ plotted in Fig. 11.

We note that our quantitative estimates for σ should be considered preliminary. All of our estimates for σ are based on square systems with $L = 64$, and assume an interface that is, on average, flat and oriented parallel to a lattice axis. A more detailed and accurate

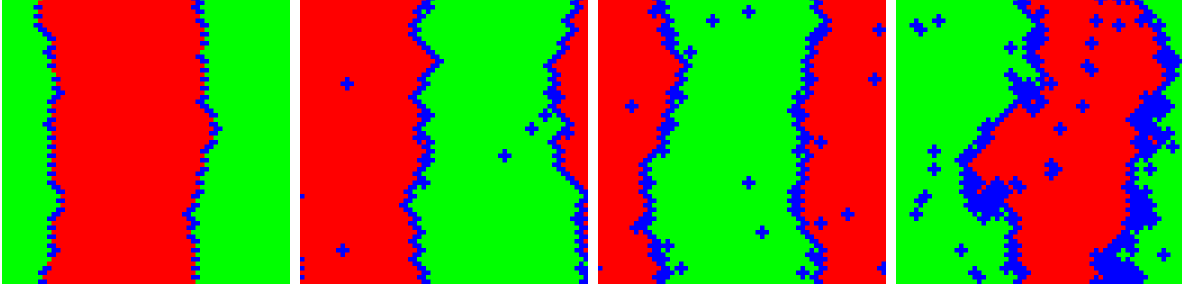


FIG. S8. Snapshots of \mathcal{AC} coexistence when $L = 64$ and $H_s = 0$ for various $H = \{1.0, 3.0, 3.5, 3.9\}$, from left to right.

analysis is possible by monitoring system-size effects, the influence of the system shape and boundary conditions, as well as considering the influence of the orientation of the interface to the lattice axes [52]. That said, for the purposes of this work, it is sufficient that we have shown that $\sigma_{AB} < \sigma_{AC}$ throughout the range of the phase diagram studied here.

Fig. S9 compares our direct numerical evaluation of $\bar{G}(n)$ at state point (f) in Table I with the CNT predictions for G_{AB} and G_{AC} as defined in Eq. 1 and calculated using the corresponding values of μ and σ given in Table I. These values of μ and σ are estimated for each phase or interface as described above. The shape of the curve for $\bar{G}(n)$ is similar to G_{AB} for $n < n_c$, and to G_{AC} for $n > n_c$, confirming the qualitative predictions of the CNT analysis in Section II. However, significant quantitative differences occur at all values of n . These differences likely arise from several sources. For example, the CNT expression in Eq. 1 for the nucleation barrier is known to deviate significantly from the numerically computed barrier even for simple lattice models such as ours [54]. Also, as noted above, we have used values of the surface tension as estimated for flat interfaces that are aligned with a lattice axis. At small n , where the interface is strongly curved, we expect this approximation to introduce significant deviations, which will manifest at larger n as an offset between the predicted and the observed curves.

S5. IDENTIFYING LOCAL FLUCTUATIONS OCCURRING WITHIN THE \mathcal{A} PHASE

Here we focus on the \mathcal{A} phase, and develop a definition for identifying local regions that deviate in structure from that expected in the \mathcal{A} phase.

In the perfect \mathcal{A} phase, all sites satisfy $s_i = -\sigma_i$. In the perfect \mathcal{C} phase, all sites satisfy

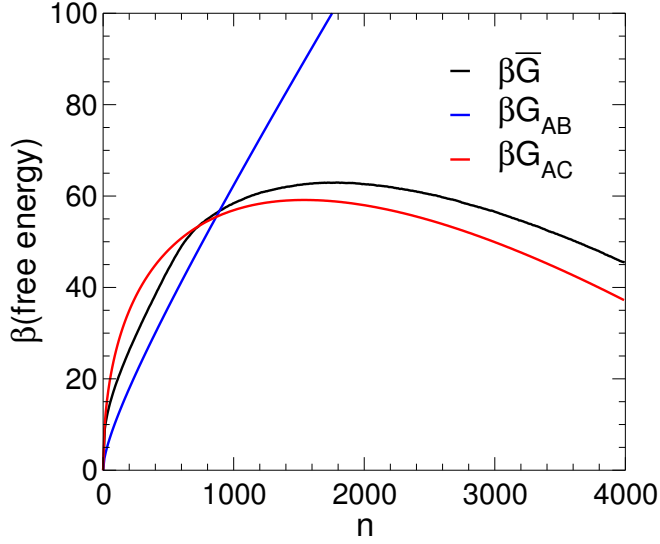


FIG. S9. Comparison of: $\bar{G}(n)$ for $L = 128$, $H=3.92$, and $H_s = 0.02$; and G_{AB} and G_{AC} as computed using Eq. 1 using the values of the chemical potentials and surface tensions as found in Table I for state point (f).

$s_i = \sigma_i$. In the perfect \mathcal{B} phase, all sites satisfy $s_i = 1$. We therefore define a local fluctuation occurring within the \mathcal{A} phase as any contiguous cluster of sites for which $s_i = \sigma_i$ or $s_i = 1$. The one exception to this definition is a single site at which $s_i = 1$ and for which all 4 nn's have $s_i = -1$. Half of the sites in the perfect \mathcal{A} phase have this property, and we exclude them from our definition of a fluctuation. An example system configuration is shown in Fig. S10, and illustrates our cluster definition.

The number of sites in a cluster is denoted by n . The number of sites in the largest cluster in the system is n_{\max} . The composition of a cluster is defined as $f = \bar{n}/n$, where \bar{n} is the number of sites in the cluster that correspond to the \mathcal{C} phase. We define $\bar{n} = 2n_{\text{down}}$, where n_{down} is the number of cluster sites for which $s_i = -1$. The reason for this definition of f is that cluster sites satisfying $s_i = 1$ may also satisfy $s_i = \sigma_i$, and so it is ambiguous if these sites belong to the fraction of sites inside the cluster that belong to the \mathcal{C} phase or to the \mathcal{B} phase. Since cluster sites with $s_i = -1$ unambiguously belong to the \mathcal{C} phase, and since the fraction of $s_i = -1$ sites in the perfect \mathcal{C} phase is $1/2$, we estimate the total number of \mathcal{C} sites within a cluster to be $2n_{\text{down}}$. The quantity f therefore characterizes the cluster composition in terms of how much of the cluster is taken up by the \mathcal{C} phase: $f = 0$

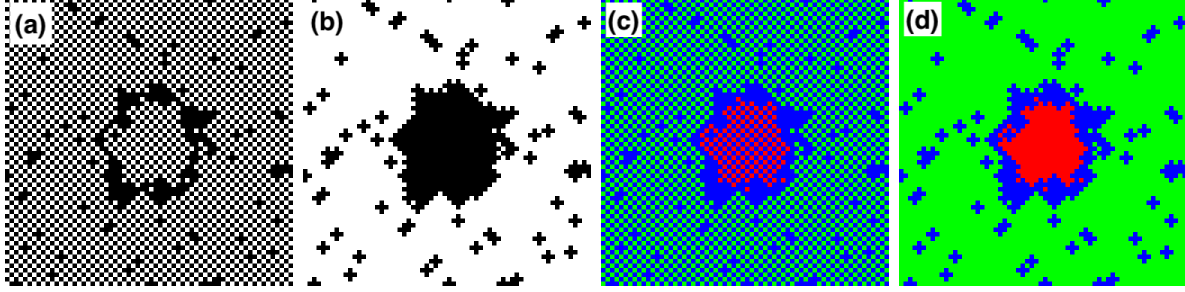


FIG. S10. Example $L = 64$ system configuration. (a) White sites satisfy $s_i = -1$. Black sites satisfy $s_i = 1$. (b) Black sites satisfy the definition for belonging to a fluctuation. White sites do not. (c) Green sites satisfy $s_i = -1 = -\sigma_i$. Blue sites satisfy $s_i = 1$. Red sites satisfy $s_i = -1 = \sigma_i$. (d) Same as (c), except that all blue sites in (c) totally surrounded by green sites are rendered as green in (d); and all blue sites in (c) totally surrounded by red sites are rendered as red in (d).

is a pure \mathcal{B} cluster, while $f = 1$ is a pure \mathcal{C} cluster.

We note that cluster sites with $s_i = 1$ on the cluster perimeter are always considered part of the cluster, even though half of them (on average) might reasonably be associated with the surrounding \mathcal{A} phase. For computational efficiency, we do not apply this correction, which if implemented would decrease the values of n and n_{\max} from those used here.

For visualization purposes, we render system configurations as shown in Fig. S10(d). The rules we use to assign a color to each site are stated in the figure caption. In the resulting color scheme, the \mathcal{A} phase is green, the \mathcal{B} phase is blue, and the \mathcal{C} phase is red.

S6. 2D UMBRELLA SAMPLING SIMULATIONS TO FIND $G(n_{\max}, f)$

$G(n_{\max}, f)$ is estimated from 2D umbrella sampling simulations using the biasing potential given in Eq. 6. We choose $\kappa_n = 0.0005$ and $\kappa_f = 500$. For each choice of (L, H_s, H, T) we conduct 900 simulations for $n_{\max}^* = 100i$ where the integer $i \in [0, 99]$, and for $f^* = j/10$ where the integer $j \in [0, 8]$. Each run is initiated from a perfect \mathcal{A} configuration, into which a seed cluster is inserted. The seed cluster is a square of sites with $s_i = 1$ of a size chosen to be closest to n_{\max}^* . At the centre of the seed cluster there is a square region with $s_i = \sigma_i$ of a size chosen so that the seed cluster has a value of f closest to f^* . This system is equilibrated for 5×10^4 MCS, and then the time series of n_{\max} and f is recorded every 100 MCS for 10^6 MCS. Trial configurations are accepted or rejected using the umbrella potential every 1 MCS. One MCS corresponds to L^2 attempts to flip the spin of a randomly chosen lattice site. Our time series for n_{\max} and f are analyzed using WHAM to evaluate $P(n_{\max}, f)$ and

$G(n_{\max}, f)$. We estimate that the error in $G(n_{\max}, f)$ is not more than $1kT$. We exclude from the WHAM analysis any run for which the acceptance rate for the umbrella sampling is less than 0.1, which occurs in a few cases when the local variation of $G(n_{\max}, f)$ is very steep. Our system size for these 2D umbrella sampling runs is $L = 128$ or 200 , as indicated in the legends or captions of the figures.

S7. 1D UMBRELLA SAMPLING SIMULATIONS TO FIND $G(n_{\max})$

To estimate n_c and n^* over a wide range of H_s and H , we conduct 1D umbrella sampling simulations in which n_{\max} alone is constrained. In this approach, we directly compute $G_1(n_{\max})$ using,

$$\beta G_1(n_{\max}) = -\log[P_1(n_{\max})] + C, \quad (\text{S19})$$

where $P_1(n_{\max})$ is proportional to the probability to observe a microstate with a given value of n_{\max} . We find n^* from the maximum in $G_1(n_{\max})$. We also monitor f during these runs, which allows us to compute χ and thus to find n_c from the maximum in χ .

To proceed, we use a biasing potential,

$$U_B'' = \kappa_n (n_{\max} - n_{\max}^*)^2, \quad (\text{S20})$$

where $\kappa_n = 0.002$. Trial configurations are accepted or rejected using the umbrella potential every 1 MCS. Each run is initiated from a perfect \mathcal{A} configuration, into which a seed cluster is inserted. The seed cluster is a square of sites with $s_i = 1$ of a size chosen to be closest to n_{\max}^* . We carry out runs using $L = 64$ or 128 , as indicated in the legends or captions of the figures. For each choice of (L, H_s, H, T) , we conduct simulations for each value of $n_{\max}^* = 50i$ where the integer $i \in [0, 24]$ when $L = 64$, and $i \in [0, 80]$ when $L = 128$. Each simulation is equilibrated for 5×10^4 MCS, and then the time series of n_{\max} is recorded every 100 MCS for 10^6 MCS. These time series are analyzed using WHAM to evaluate $P_1(n_{\max})$ and $G_1(n_{\max})$. We exclude from the WHAM analysis any runs for which the acceptance rate for the umbrella sampling is less than 0.1. As shown in Fig. 12, we use these 1D umbrella sampling runs to evaluate n_c and n^* for H_s in the range $[0.01, 0.10]$ and H in the range $[3.7, 4.0]$.

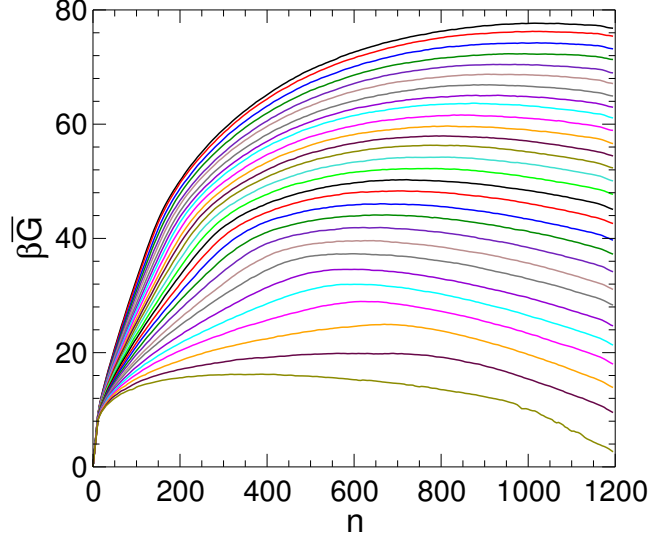


FIG. S11. $\bar{G}(n)$ for $L = 64$ and $H_s = 0.04$. $H = 3.70$ to 3.97 in steps of 0.01 , from top to bottom.

S8. HEIGHT OF THE NUCLEATION BARRIER

An example of the data used to find the locus along which $\beta G^* = 20$ is shown in Fig. S11. Here we show $\bar{G}(n)$ for several values of H at $H_s = 0.04$. We obtain G^* from the maxima of these curves, and by interpolation identify the value of H at which $\beta G^* = 20$. The locus of points in the (H_s, H) plane at which $\beta G^* = 20$ is shown in Fig. 2.

S9. FINDING n_c FROM χ

Fig. S12(a) reproduces the data for G_B and G_C from Fig. 9(a), in which the crossing of these two curves identifies n_c . Fig. S12(b) shows χ as a function of n_{\max} for the same three cases shown in Fig. S12(a). We find that the maximum of χ corresponds within error to the value of n_c obtained by finding the intersection of G_B and G_C . Based on this correspondence, all values of n_c reported in this work are computed by finding the maximum of χ . This definition allows us to estimate n_c from both 1D and 2D umbrella sampling simulations.

S10. ADDITIONAL PLOTS OF $G(n_{\max}, f)$

We present in Figs. S13 and S14 surface and contour plots of $G(n_{\max}, f)$ over additional values of H between 3.960 and 3.985 .

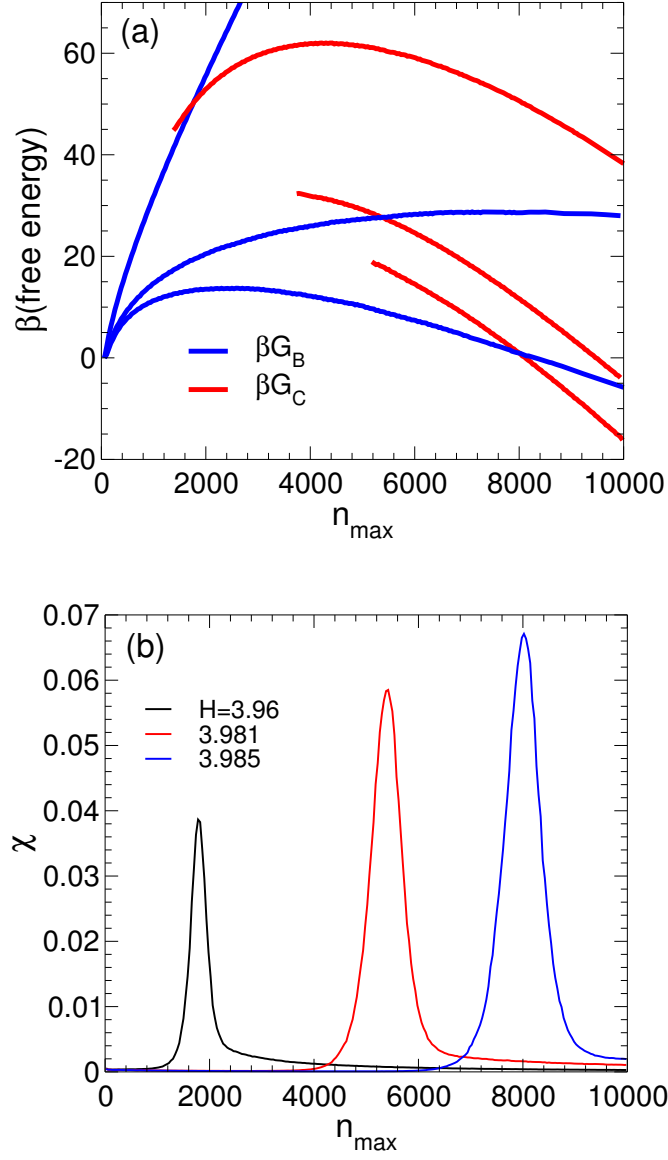


FIG. S12. (a) G_B and G_C for $H_s = 0.01$ and $L = 200$. From top to bottom $H = \{3.96, 3.981, 3.985\}$
 (b) χ for $H_s = 0.01$ and $L = 200$. From left to right $H = \{3.96, 3.981, 3.985\}$.

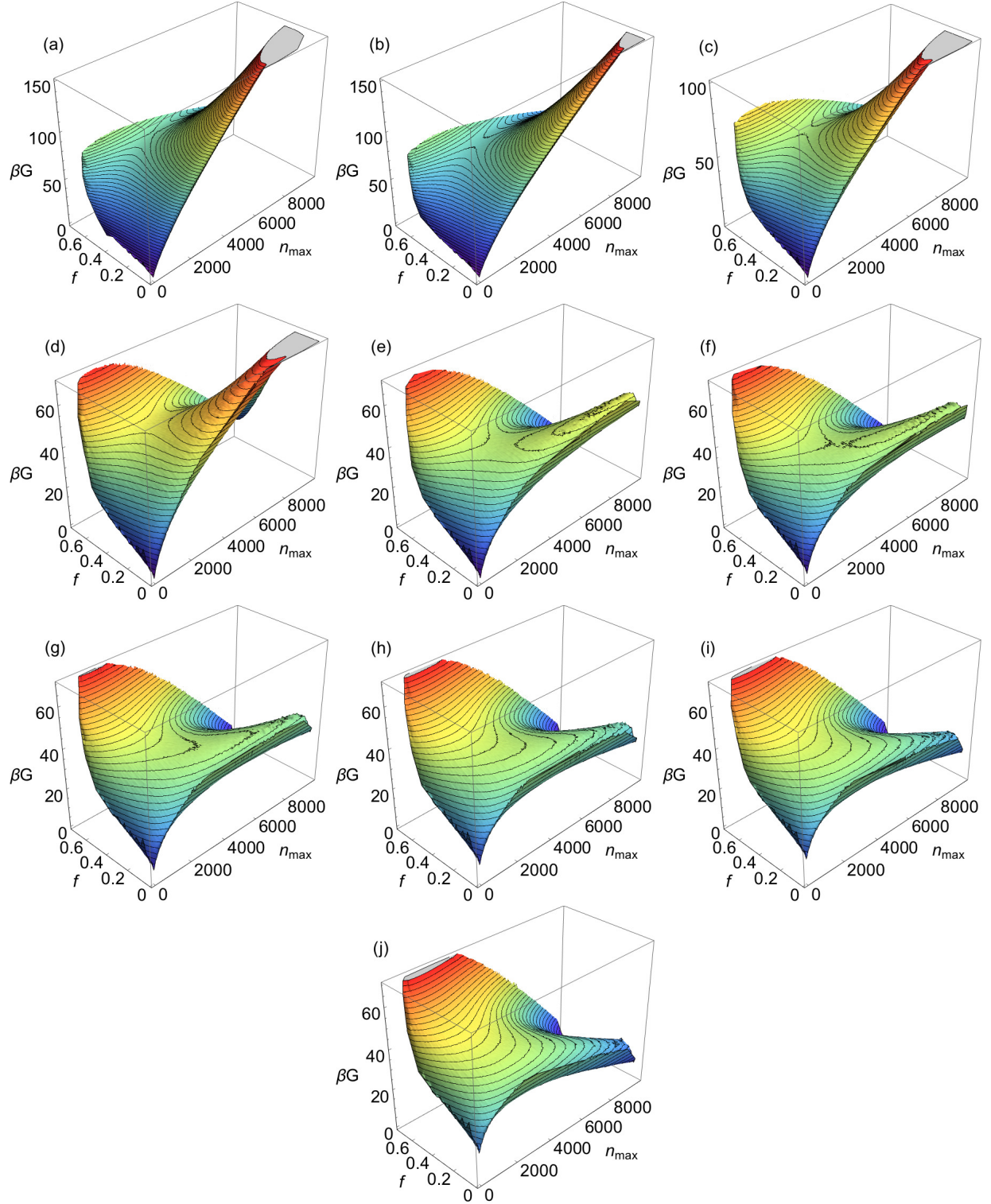


FIG. S13. $G(n_{\max}, f)$ for $H_s = 0.01$ and $L = 200$. Panels (a) through (j) correspond respectively to $H = \{3.96, 3.965, 3.97, 3.975, 3.98, 3.981, 3.982, 3.983, 3.984, 3.985\}$. Contours are $2kT$ apart.

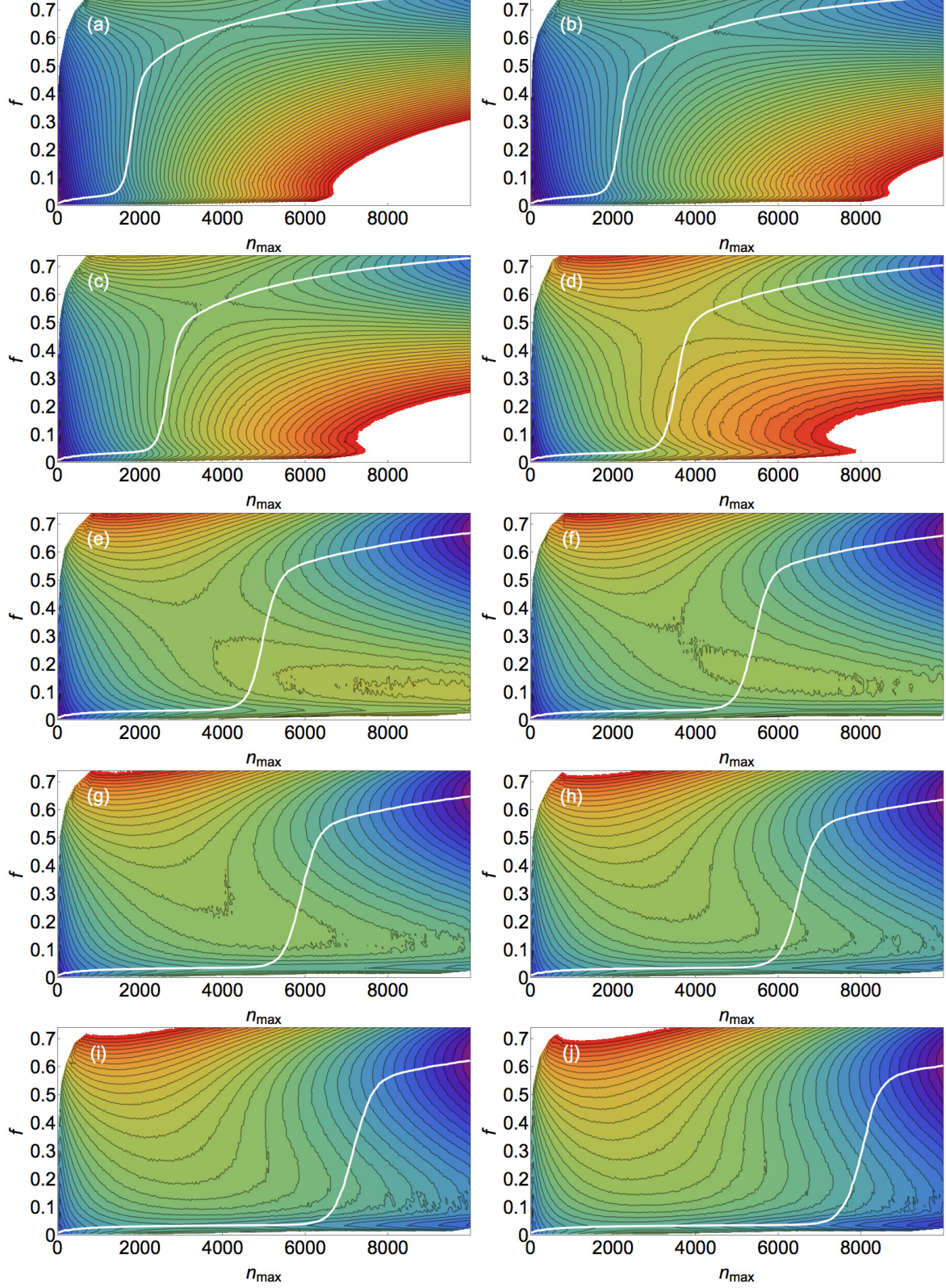


FIG. S14. $G(n_{\max}, f)$ for $H_s = 0.01$ and $L = 200$. The white line is $\langle f \rangle$. Panels (a) through (j) correspond respectively to $H = \{3.96, 3.965, 3.97, 3.975, 3.98, 3.981, 3.982, 3.983, 3.984, 3.985\}$. Contours are $2kT$ apart.